Theor. Comput. Fluid Dyn. (2017) 31:89–110
DOI 10.1007/s00162-016-0407-8

ORIGINAL ARTICLE

Michèle De La Chevrotière · Boualem Khouider

A zonally symmetric model for the monsoon-Hadley circulation with stochastic convective forcing

Received: 16 May 2016 / Accepted: 19 August 2016 / Published online: 9 September 2016

Abstract Idealized models of reduced complexity are important tools to understand key processes underlying a complex system. In climate science in particular, they are important for helping the community improve our ability to predict the effect of climate change on the earth system. Climate models are large computer codes based on the discretization of the fluid dynamics equations on grids of horizontal resolution in the order of 100 km, whereas unresolved processes are handled by subgrid models. For instance, simple models are routinely used to help understand the interactions between small-scale processes due to atmospheric moist convection and large-scale circulation patterns. Here, a zonally symmetric model for the monsoon circulation is presented and solved numerically. The model is based on the Galerkin projection of the primitive equations of atmospheric synoptic dynamics onto the first modes of vertical structure to represent free tropospheric circulation and is coupled to a bulk atmospheric boundary layer (ABL) model. The model carries bulk equations for water vapor in both the free troposphere and the ABL, while the processes of convection and precipitation are represented through a stochastic model for clouds. The model equations are coupled through advective nonlinearities, and the resulting system is not conservative and not necessarily hyperbolic. This makes the design of a numerical method for the solution of this system particularly difficult. Here, we develop a numerical scheme based on the operator time-splitting strategy, which decomposes the system into three pieces: a conservative part and two purely advective parts, each of which is solved iteratively using an appropriate method. The conservative system is solved via a central scheme, which does not require hyperbolicity since it avoids the Riemann problem by design. One of the advective parts is a hyperbolic diagonal matrix, which is easily handled by classical methods for hyperbolic equations, while the other advective part is a nilpotent matrix, which is solved via the method of lines. Validation tests using a synthetic exact solution are presented, and formal second-order convergence under grid refinement is demonstrated. Moreover, the model is tested under realistic monsoon conditions, and the ability of the model to simulate key features of the monsoon circulation is illustrated in two distinct parameter regimes.

Keywords Climate science · Reduced models · Monsoon · Hyperbolic equations · Numerical methods stochastic convection · Hadley circulation

Mathematics Subject Classification 35L02 · 65C20 · 65C35 · 65M08 · 65M30 · 65Z99 · 86A10

Communicated by Dr. Rupert Klein.

M. De La Chevrotière · B. Khouider
Department of Mathematics and Statistics, University of Victoria, PO Box 3060 STN CSC, Victoria, BC V8W 3P4, Canada

Present Address:
M. De La Chevrotière (✉)
Department of Mathematics, Pennsylvania State University, University Park, PA 16802, USA
E-mail: mdelachev@psu.edu

1 Introduction

Climate change remains one of the grand challenges of the century for humankind, despite continued international efforts on various fronts, such as coordinated policies for reducing greenhouse gas emissions or the constant search for sustainable/renewable energy sources. Yet the actual impact of global warming and its effect on local weather and climate remain poorly understood due in part to major uncertainties in the current computer models used for long term weather and climate predictions, known by the generic names of global climate models (GCMs) or earth system models (ESMs).

GCMs and ESMs are based on a discretization of the 3D governing fluid equations for the atmosphere and the oceans, known as the Navier–Stokes equations, forced by various external processes such as solar radiation, Earth topography, and the ice and vegetation covers [22,37,51,58]. The climate system dynamics involves a hierarchy of scales ranging from a few micrometers and milliseconds due to processes such as condensation and cloud droplet interactions, to planetary-scale oscillations with periods of months to decades. Atmosphere and ocean turbulent flows and waves of various sorts fill up this wide spectrum and exchange energy and momentum via strong nonlinear interactions that cannot be ignored. However, due to limitations in computing power, only a small range of these scales can be represented at once in a climate or weather forecasting simulation. For instance, climate simulations spanning several years to a few decades have horizontal resolution around 100–200 km, and processes occurring at that grid scale or smaller are represented by various closure recipes known as parameterizations [4,58].

One of the climate model biases of paramount importance is their inability to predict the distribution and variability of rainfall patterns, especially in the tropics [43]. This adds to the uncertainty in using the model predictions for policy making by government officials. The dominant precipitation events in the tropics occur in association with organized deep convection, which is believed to be the Achilles's heel of climate models [46]. The challenge arises because tropical convection involves a hierarchy of scales ranging from the convective cloud or cell of a few kilometers to mesoscale cloud clusters of around 100–500 km, which are modulated by synoptic (1000–5000 km) and planetary ($\geq$10,000 km) scale waves [34,48]. A good understanding of the interaction of organized tropical convection and clouds in general with large-scale atmospheric and oceanic circulation patterns is not only an interesting scientific issue but also an important one since it contributes to the improvement of climate models. Such understanding is often gained through the analysis of observational data generated by massive collections of satellite images [63], or meticulously designed and executed field campaigns [64,65], or the design and study of process oriented simplified numerical models [16,20,21,34,49].

An important force that drives atmospheric and oceanic flows is induced by the differential stress imposed by the rotation of the Earth, due to its curvature, known as the Coriolis force [22]. In the midlatitudes, where the Coriolis force is nonzero, synoptic-scale atmospheric and oceanic flows are always in a state of near equilibrium, known as the quasi-geostrophic (QG) balance, where the pressure gradient is balanced by this Coriolis force [22]. This state of affairs allowed early meteorologists to gain a good understanding of the formation and propagation of midlatitude weather systems and even allowed the fabrication of the first prototype of numerical weather prediction models, via the use of what is known as the QG equations [22,47]. The QG equations are equivalent in complexity to the 2D Euler equations [5], which is a huge simplification from the global 3D primitive equations. However, because the Coriolis force vanishes and changes sign at the Equator, the QG equations break down in the tropics and the Equator acts as a wave guide for a large spectrum of waves that are trapped near and travel along the Equator in both East and West directions [17,47]. Not surprisingly, the design and study of simple models to study the interactions of equatorial waves with each other, with convection, and with extra-tropical and planetary motions are a very active research area [34,36,39].

On top of its extraordinarily rich wave activity, the tropical atmosphere harbors a multitude of mean flow circulation patterns due essentially to the nonisotropic solar radiation intake, the geographic distribution of oceanic warm waters and topography, and their interactions with the Coriolis force. The mean rainfall, for instance, shows a long band of intense activity, which extends along the Indian and the Pacific Oceans and through a large portion of the tropical Atlantic and Africa. This elongated region of intense precipitation is known as the intertropical convergence zone (ITCZ), which, on average, is characterized by the raising of warm and moist air, which then cools and dries and descends a few thousands of kilometers on its Northern and Southern flanks, resulting in some of the driest deserts on Earth such as the Sahara and the Australian Outbacks. The associated circulation, closed through converging air near the surface and divergence aloft, is known as the Hadley circulation [2,17,34,45]. Because the maximum incoming solar radiation moves North–South between the two hemispheres throughout the year, resulting in the four seasons, the ITCZ lies North of the Equator

during the northern hemisphere summer and right at or somewhat South of the Equator during winter. The northward migration of the ITCZ results in a phenomenal shift in winds and precipitation patterns so that, over the Arabian sea for instance, southwesterly winds prevail during summer and northeasterlies prevail during winter, connecting back and forth the Indian continent and the Somali Coast [39]. Also, this northern migration coincides with the Indian rainy season where tremendous amounts of rain fall over the continent, without which India will be just a large hot desert much like the Sahara. This climate phenomenon is known as the monsoon, from the Arabic word for season, most likely coined by Arab sailors and merchants. The amount of rain that falls during one monsoon season, its timing, and its frequency are of paramount importance for the Indian agriculture, economy, and society as a whole [38]. Nonetheless, the monsoon phenomenon is predominant in many other locations that have similar geographic conditions as the Indian continent (a land mass located poleward of a tropical ocean basin) with the same consequences, including all the West African countries surrounding the Gulf of Guinea, Northern Australia, and Southern United States, and the Gulf of Mexico [39].

In this work, we develop a zonally symmetric numerical model for the large-scale Hadley circulation, ambient winds, and precipitation associated with the summer monsoon season. The planetary-scale atmospheric circulation is coupled with both the small-scale processes of deep convection and the boundary layer dynamics that sustains shallow convection. This axially symmetric model allows to study the propagation and initiation of convection and its interaction with the large-scale circulation without the effects of zonally propagating atmospheric waves. Such axially symmetric models have been used by several authors to study meridional circulation features and Hadley-monsoon dynamics. For instance, Drbohlav and Wang [14] emphasized the importance of the barotropic and baroclinic modes in the propagation and initiation of convection and studied monsoon intraseasonal oscillation using a 2D axially symmetric model. Pauluis [53] used an axisymmetric model to investigate the role of the atmospheric boundary layer in the Hadley circulation. See also the pioneering work of Webster, Goswami and co-workers [20,62, for example]. However, these models use simple deterministic parameterizations of convection, which revealed to be inadequate for organized tropical convection [43,48] or a fewer vertical modes. The model in [14], for instance, is based on two free tropospheric layers and one boundary layer and uses a moisture convergence convection scheme, while the model in [53] uses the Emanuel parameterization scheme and is based on a fully resolved numerical model for the free troposphere plus a bulk mixed boundary layer. The model proposed here is based on a new stochastic convection scheme, which proved to be successful in the representation of some key features of tropical wave dynamics including the monsoon [2,3,11,12,27,35, etc.].

The present model is based on the multicloud model (MCM) of Khouider and Majda [30,32], which was originally proposed to study convectively coupled equatorial waves and later used successfully as a cumulus parameterization in a GCM [35]. Here we extend the MCM to include the dynamical effects of atmospheric boundary layer (ABL) turbulence and shallow convection. The ABL model was proposed and studied by Waite and Khouider [61] in the linear case and with a deterministic convective parameterization. It is shown in [61] that the boundary layer coupling enhances the instability of convectively coupled waves by enforcing ABL convergence and mechanical coupling between the ABL and the free troposphere and is essential for modeling the diurnal cycle of precipitation over land and over the ocean [15]. However, unlike the aforementioned work, here the convection processes are represented by the stochastic multicloud (SMCM) of Khouider et al. [27] with its key timescale parameters inferred from a large eddy simulation [25] of convection over the tropical Atlantic ocean by De La Chevrotiere et al. [10].

We note that the main novelties here are multifold. Firstly, this is the first time that the multicloud model with a dynamical boundary layer is considered with all nonlinear advection terms retained. Secondly, it is also the first time that this four-layer model is coupled to the SMCM. Thirdly, unlike previous studies where zonal flows along the Equator were considered in order to study convectively coupled equatorial waves, here, as already pointed out, we consider the zonally symmetric case of North–South-oriented flows, especially associated with monsoon conditions, i.e., when the sea-surface warm pool is moved a significant distance North of the Equator.

This work is motivated by ongoing efforts of several research groups to implement the SMCM in operational climate models to improve their forecasting skills in terms of tropical weather and climate, especially associated with tropical waves and monsoons [1–3,11–13,54,55]. Studies based on simplified models such as the one presented here would contribute enormously not only toward our understanding of how the SMCM interacts with the large-scale circulation in the GCM context, but also serve as road maps for its effective implementation in operational models. Building model hierarchies with increasing complexity is important when dealing with complex systems such as the Earth's climate, since the simpler models can be used to draw conclusions about the results obtained from the more complex ones [21]. However, because the present model, although

simplified, remains fairly complex and particularly highly nonlinear, this paper is mainly concerned with the design and implementation of a numerical solution strategy for the simplified model, though some discussion is provided near the end to demonstrate its performance in two distinct parameter regimes.

The simplified dynamical model starts with a Galerkin projection of the governing equations into the three first modes of vertical structure in the free troposphere: the zeroth or barotropic mode, which is uniform in the vertical, and the first and second baroclinic modes whose horizontal velocity vertical structures consist of a half cosine shear and a full cosine jet shear, respectively. The corresponding vertical velocity and temperature anomalies consistently follow half-sine and full-sine profiles, respectively. The ABL is represented through bulk equations derived via a systematic vertical averaging of the primitive equations from the surface to an assumed fixed ABL height, h_b.

As already stated above, while the model setting and derivation follow the work of Waite and Khouider [61], here we are interested in the North–South (meridional) circulation in the presence of a summer ITCZ as a boundary value problem with the full nonlinear advection terms, while previous studies [30, for example] were concerned solely by zonal (East–West) linear wave dynamics forced by convection. Moreover, as already mentioned, this is the first time the coupled SMCM-ABL model is considered. Previously, Khouider and Majda [28] considered the full 2D case for the 2 modes model reduced to a barotropic and a first baroclinic mode, and Stechmann et al. [57] studied the case of nonlinearly coupled first and second baroclinic modes. This is the first time all four modes (ABL, barotropic and first two baroclinic) are coupled together through advective nonlinearities. A common feature of these coupled vertical mode derivations is that they all result in partial differential systems of first order that are neither conservative nor strictly hyperbolic. Following in the steps of [28,57], a numerical methodology for solving the coupled system is designed and validated. As in [28] and [57], we adopt a time-splitting strategy where the coupled system is divided into a conservative part, a hyperbolic part, and a nilpotent part so that each component can be handled with its own appropriate numerical scheme to preserve both numerical stability and key physical properties [28,57].

The paper is organized as follows: In Sect. 2, we expose the derivation of the three vertical modes model coupled through nonlinear advection for the monsoon circulation, and its coupling to the bulk boundary layer dynamics. This is followed by a discussion of the Markov chain SMCM for convective forcing and its two-way coupling with the large-scale dynamics. In Sect. 3, we present the numerical strategy of splitting the model equations into various components that can be handled transparently with state-of-the-art numerical methods. We then report some validation test results in the form of numerical convergence under grid refinement for the model dry dynamics, i.e., without convective forcing or moisture coupling. Finally, we end the paper with some concluding remarks in Sect. 5.

2 Model derivation and stochastic convective forcing

Here, we describe the derivation of the zonally symmetric model for the monsoon with a crude vertical resolution, reduced to the barotropic and the first two baroclinic modes in the free troposphere and a bulk, vertically averaged, model for the boundary layer. This is followed by the stochastic model for convection and its two-way coupling to the large-scale equations.

2.1 The zonally symmetric model with a mechanical boundary layer

We consider the hydrostatic Boussinesq equations on the equatorial β-plane for the free troposphere [17, 47], with zonal symmetry, i.e., neglecting zonal advection and East–West propagating waves. These are in nondimensional form:

$$\frac{\partial u}{\partial t} + v\frac{\partial u}{\partial y} + w\frac{\partial u}{\partial z} - yv = \mathcal{S}^u, \tag{1a}$$

$$\frac{\partial v}{\partial t} + v\frac{\partial v}{\partial y} + w\frac{\partial v}{\partial z} + yu = -\frac{\partial p}{\partial y} + \mathcal{S}^v, \tag{1b}$$

$$\frac{\partial p}{\partial z} = \theta, \tag{1c}$$

$$\frac{\partial \theta}{\partial t} + v\frac{\partial \theta}{\partial y} + w\frac{\partial \theta}{\partial z} + w = \mathcal{H}^\theta + \mathcal{S}^\theta, \tag{1d}$$

$$\frac{\partial v}{\partial y} + \frac{\partial w}{\partial z} = 0. \tag{1e}$$

Here y and z are, respectively, the meridional and vertical coordinates with positive directions from South to North, and bottom to top, respectively; $t > 0$ is time. The free troposphere is capped with the tropopause at height $H_T = 16\,\text{km}$, and sits on top of an atmospheric boundary layer (ABL) of depth $h_b = 500\,\text{m}$. For convenience, the free troposphere and ABL have dimensional vertical extents of $0 \le z \le H_T$ and $-h_b \le z \le 0$, respectively, so that the top of the ABL is located at $z = 0$ and the Earth's surface at $z = -h_b$. The horizontal velocity $\boldsymbol{u} = (u, v)$ has zonal (along the Equator) component u and meridional (North–South) component v. The vertical velocity is w. The scalars p and θ are the pressure and potential temperature (i.e., the temperature that a parcel of air would have if displaced adiabatically to a reference pressure) perturbations, respectively. The effective total potential temperature θ_{tot} is expressed in dimensional units as $\theta_{\text{tot}}(y, z, t) = \theta_{\text{ref}} + \theta_0(z) + \theta(y, z, t)$, where $\theta_{\text{ref}} = 300\,\text{K}$ is a reference potential temperature, θ_0 sets the background stratification, and θ is the (dimensional) deviation from this background. The background state θ_0 is based on an assumed linear stratification with a constant Brunt–Väisälä buoyancy frequency N_v, given by

$$N_v^2 = \frac{g}{\theta_{\text{ref}}} \frac{\mathrm{d}\theta_0}{\mathrm{d}z} = 10^{-4}\,\text{s}^{-2}, \tag{2}$$

where $g = 9.8\ \text{ms}^{-2}$ is the gravitational acceleration.

For simplicity, the zonal pressure differential is neglected. The forcing terms $\mathcal{S}^u$, $\mathcal{S}^v$, $\mathcal{H}^\theta$ and $\mathcal{S}^\theta$ represent the sources and sinks of zonal and meridional momentum, and potential temperature, respectively. In particular, $\mathcal{S}^\theta$ includes heating and cooling resulting from convective and radiative processes, which will be specified through the stochastic cloud model below.

The equations in (1) are written in nondimensional units using equatorial synoptic dynamic scales as a reference, such that both the gradient of the Coriolis parameter $f(y) = 2\Omega \sin(y)$ (Ω is the Earth's rotational frequency) at the Equator,

$$\beta = \left.\frac{\partial f(y)}{\partial y}\right|_{y=0} = 2.28 \times 10^{-11}\ \ \text{m}^{-1}\text{s}^{-1}, \tag{3}$$

and the buoyancy frequency (2) are unity [47]. The first baroclinic dry gravity wave speed $c = N_v H_T/\pi \approx 50$ ms^{-1} and the equatorial Rossby deformation radius $L = \sqrt{c/\beta} \approx 1500\,\text{km}$ are the horizontal velocity and length scales, respectively. We use $T = L/c \approx 8\,\text{h}$ as the timescale, and the dry static stratification $\alpha = H_T N_v^2 \theta_{\text{ref}}/\pi g \approx 15\,\text{K}$ as the temperature scale. For convenience, the vertical length scale is set to H_T/π and the free troposphere vertical velocity scale is given by $\nu = H_T/T\pi \approx 0.17\,\text{m/s}$ (Table 1). Consistently, the mass-weighted pressure scale is c^2. The equations in (1) are supplemented with rigid lid boundary conditions at the top of the troposphere ($z = \pi$) and at the Earth's surface ($z = -\delta\pi$), that is,

$$w\big|_{z=\pi,\,-\delta\pi} = 0, \tag{4}$$

where $\delta = h_b/H_T$ is the ratio between the ABL and free tropospheric heights.

The full model for the atmosphere incorporates a free troposphere, whose vertical structure is truncated to the first three internal normal modes, sitting on top of a mixed ABL, described by a bulk dynamical model. The equations for the free troposphere are systematically coupled to the ABL equations by assuming continuity of pressure and vertical velocity across the fixed interface, located at $z = 0$:

$$\lim_{z\to 0^+} w(y, z, t) = w_t, \quad \lim_{z\to 0^+} p(y, z, t) \equiv p_t, \tag{5}$$

where w_t and p_t are the vertical velocity and pressure at the top of the ABL (the subscript t should not be confounded with a time derivative). As a consequence, the ABL vertical velocity is a source of divergence of the horizontal component of the barotropic flow in the troposphere [see (9)]. This nonzero divergence of the troposphere horizontal barotropic flow leads to (i) important contributions to the free troposphere equations through vertical advection and (ii) a nontrivial Poisson pressure equation, presented in Sect. 2.2.

Table 1 Troposphere model parameters and scaling factors

Parameter or Scaling factors	Derivation	Approximate value	Description
H_T		16 km	Tropopause height
θ_{ref}		300 K	Reference potential temperature
g		9.8 m/s	Gravitational acceleration
θ_0		Function of height z	Background potential temperature, in K
N_v	$\sqrt{\frac{g}{\theta_{\text{ref}}}\frac{\mathrm{d}\theta_0}{\mathrm{d}z}}$	10^{-2} s^{-1}	Brunt-Väisälä buoyancy frequency
c	$N_v H_T/\pi$	50 m/s	Horizontal velocity scale
β	$\left.\frac{\partial f(y)}{\partial y}\right\|_{y=0}$	2.28×10^{-11} m^{-1}s^{-1}	Variation of Coriolis parameter f at the Equator
L	$\sqrt{c/\beta}$	1500 km	Equatorial Rossby deformation radius/ Horizontal length scale
T	L/c	8 h	Reference timescale
α	$\frac{H_T N_v^2 \theta_{\text{ref}}}{\pi g}$	15 K	Potential temperature scale
v	$\frac{H_T}{\pi T}$	0.17 m/s	Free troposphere vertical velocity scale

Following [61], we impose the following ansatz of truncating the free troposphere wave dynamics to the first three modes of vertical structure:

$$\begin{pmatrix} \boldsymbol{u} \\ p \end{pmatrix}(y,z,t) = \begin{pmatrix} \boldsymbol{u}_0 \\ p_0 \end{pmatrix}(y,t) + \begin{pmatrix} \boldsymbol{u}_1 \\ p_1 \end{pmatrix}(y,t)C_1(z) + \begin{pmatrix} \boldsymbol{u}_2 \\ p_2 \end{pmatrix}(y,t)C_2(z), \tag{6}$$

$$\begin{pmatrix} \theta \\ w \end{pmatrix}(y,z,t) = \begin{pmatrix} 0 \\ w_0(y,z,t) \end{pmatrix} + \begin{pmatrix} \theta_1 \\ w_1 \end{pmatrix}(y,t)S_1(z) + \begin{pmatrix} 2\theta_2 \\ w_2 \end{pmatrix}(y,t)S_2(z), \tag{7}$$

for $0 \le z \le \pi$. Here $S_j(z) = \sqrt{2}\sin(jz)$ and $C_j(z) = \sqrt{2}\cos(jz)$, $0 \le z \le \pi$, $j = 1, 2$, are the Galerkin truncation basis functions associated with the first and second baroclinic modes of vertical structure [47]. The zeroth-barotropic mode is set to $C_0(z) = 1$, for $0 \le z \le \pi$. The factors $\sqrt{2}$ are added to obtain an orthonormal basis in the L_2 inner product $\langle F, G\rangle = \frac{1}{\pi}\int_0^\pi F(z)G(z)\mathrm{d}z$, that is, $\langle C_i, C_j\rangle = \delta_{ij}$ and $\langle S_i, S_j\rangle = \delta_{ij}$. The horizontal velocity and potential temperature structures associated with these three modes are illustrated in Fig. 1. The potential temperature and vertical velocity baroclinic wave amplitudes are found by substituting (6) and (7) into the hydrostatic equation (1c) and the incompressibility condition (1e):

$$\theta_j = -p_j, \quad w_j = -\frac{1}{j}\frac{\partial v_j}{\partial y}, \quad j = 1, 2. \tag{8}$$

As mentioned earlier, the nonvanishing free troposphere vertical velocity at the lower boundary (5) induces an active "barotropic" component

$$w_0(y,z,t) = \frac{\partial v_0}{\partial y}(y,t)(\pi - z), \quad 0 \le z \le \pi. \tag{9}$$

To see this, first integrate the divergence equation (1e) with the ansatz (6) and apply the boundary condition at top of the troposphere (4). Projecting the divergence equation (1e) onto the barotropic mode now gives

$$\frac{\partial v_0}{\partial y} = \frac{1}{\pi}w_t = -\delta\frac{\partial v_b}{\partial y}. \tag{10}$$

The vertical structure profiles of the coupled free troposphere-ABL model are depicted in Fig. 2.

A systematic Galerkin projection procedure applied to the zonally symmetric primitive equations (1) onto the modes C_j, S_j, $j = 0, 1, 2$, yields the following system of eight equations:

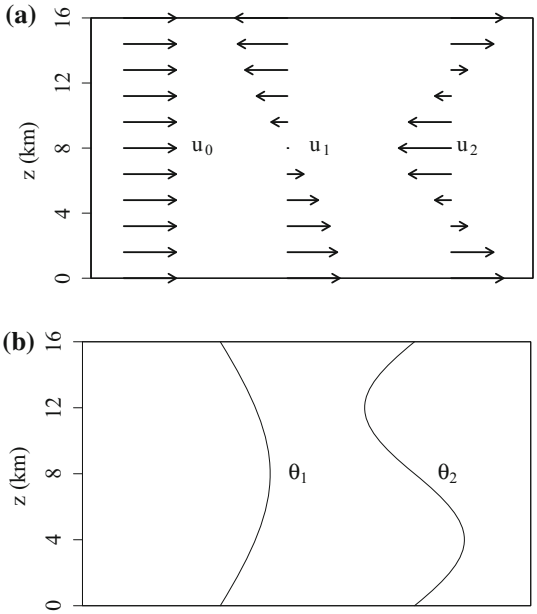

Fig. 1 Vertical structure for the horizontal velocity and potential temperature θ associated with the barotropic and first and second baroclinic modes. **a** Barotropic mode u_0 and first two baroclinic modes u_1 and u_2. **b** First two baroclinic modes θ_1 and θ_2

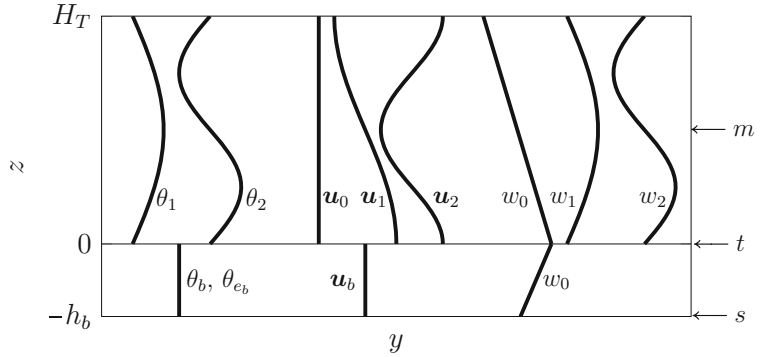

Fig. 2 Vertical structure of the model. The subscripts s, t and m indicate vertical levels located at the *surface*, *top* of the ABL, and *middle* troposphere, respectively

$$\frac{D_0 u_0}{Dt} + \frac{\partial\,(u_1 v_1)}{\partial y} + \frac{\partial\,(u_2 v_2)}{\partial y} - \sqrt{\mathbf{2}}(\boldsymbol{u_1} + \boldsymbol{u_2})\frac{\boldsymbol{\partial v_0}}{\boldsymbol{\partial y}} - y v_0 = \mathcal{S}_0^u,$$

$$\frac{D_0 v_0}{Dt} + \frac{\partial(v_1^2)}{\partial y} + \frac{\partial(v_2^2)}{\partial y} - \sqrt{\mathbf{2}}(\boldsymbol{v_1} + \boldsymbol{v_2})\frac{\boldsymbol{\partial v_0}}{\boldsymbol{\partial y}} + y u_0 = -\frac{\partial p_0}{\partial y} + \mathcal{S}_0^v,$$

$$\frac{D_0 u_1}{Dt} + v_1\frac{\partial u_0}{\partial y} + \frac{\sqrt{2}}{2}\left(v_1\frac{\partial u_2}{\partial y} + v_2\frac{\partial u_1}{\partial y} + 2u_2\frac{\partial v_1}{\partial y} + \frac{1}{2}u_1\frac{\partial v_2}{\partial y}\right) - \left(\frac{\mathbf{1}}{\mathbf{2}}\boldsymbol{u_1} + \frac{\mathbf{8}}{\mathbf{3}}\boldsymbol{u_2}\right)\frac{\boldsymbol{\partial v_0}}{\boldsymbol{\partial y}} - y v_1 = \mathcal{S}_1^u,$$

$$\frac{D_0 v_1}{Dt} + v_1\frac{\partial v_0}{\partial y} + \frac{\sqrt{2}}{2}\left(v_1\frac{\partial v_2}{\partial y} + v_2\frac{\partial v_1}{\partial y} + 2v_2\frac{\partial v_1}{\partial y} + \frac{1}{2}v_1\frac{\partial v_2}{\partial y}\right) - \left(\frac{\mathbf{1}}{\mathbf{2}}\boldsymbol{v_1} + \frac{\mathbf{8}}{\mathbf{3}}\boldsymbol{v_2}\right)\frac{\boldsymbol{\partial v_0}}{\boldsymbol{\partial y}} + y u_1 = \frac{\partial \theta_1}{\partial y} + \mathcal{S}_1^v,$$

$$\frac{D_0 \theta_1}{Dt} - \frac{\partial v_1}{\partial y} + \frac{\sqrt{2}}{2}\left(2v_1\frac{\partial \theta_2}{\partial y} - v_2\frac{\partial \theta_1}{\partial y} + 4\theta_2\frac{\partial v_1}{\partial y} - \frac{1}{2}\theta_1\frac{\partial v_2}{\partial y}\right) + \left(\frac{\mathbf{1}}{\mathbf{2}}\boldsymbol{\theta_1} - \frac{\mathbf{8}}{\mathbf{3}}\boldsymbol{\theta_2}\right)\frac{\boldsymbol{\partial v_0}}{\boldsymbol{\partial y}} + \sqrt{\mathbf{2}}\frac{\boldsymbol{\partial v_0}}{\boldsymbol{\partial y}} = \mathcal{H}_1^\theta + \mathcal{S}_1^\theta,$$

$$\frac{D_0 u_2}{Dt} + v_2\frac{\partial u_0}{\partial y} + \frac{\sqrt{2}}{2}\left(v_1\frac{\partial u_1}{\partial y} - u_1\frac{\partial v_1}{\partial y}\right) + \left(\frac{\mathbf{2}}{\mathbf{3}}\boldsymbol{u_1} - \frac{\mathbf{1}}{\mathbf{2}}\boldsymbol{u_2}\right)\frac{\boldsymbol{\partial v_0}}{\boldsymbol{\partial y}} - y v_2 = \mathcal{S}_2^u,$$

Table 2 Closure equations for convective and turbulent mixing forcing terms

Forcing term	Closure equation
Momentum turbulent drag for barotropic mode	$\mathcal{S}_0^{\boldsymbol{u}} = \delta E_{\boldsymbol{u}} \Delta_t \boldsymbol{u}$
Momentum turbulent drag for baroclinic modes	$\mathcal{S}_j^{\boldsymbol{u}} = \frac{\sqrt{2}\delta}{\tau_T} \Delta_t \boldsymbol{u} - \frac{1}{\tau_R} \boldsymbol{u}_j, \ j = 1, 2$
Velocity jump at top of boundary layer	$\Delta_t \boldsymbol{u} = \boldsymbol{u}_b - \boldsymbol{u}_t = \boldsymbol{u}_b - \boldsymbol{u}_0 - \sqrt{2}(\boldsymbol{u}_1 + \boldsymbol{u}_2)$
First baroclinic convective heating	$\mathcal{H}_1^{\theta} = H_d$
Deep convection[a]	$H_d = \left\{ \sigma_d \overline{Q} + \frac{\sigma_d}{\overline{\sigma_d \tau_c^0}} \left[a_1 \theta'_{eb} + a_2 q' - a_0 (\theta'_1 + \gamma_2 \theta'_2) \right] \right\}^+$
Second baroclinic convective heating	$\mathcal{H}_2^{\theta} = H_c - H_s$
Stratiform heating	$H_s = \frac{\sigma_s \alpha_s}{H_m} \sqrt{\text{CAPE}^+}$
Convective available potential energy[a]	$\text{CAPE} = \overline{CAPE} + R[\theta'_{eb} - a'_0(\theta'_1 + \gamma_2 \theta'_2)]$
Congestus heating	$H_c = \frac{\sigma_c \alpha_c}{H_m} \sqrt{\text{CAPE}_l^+}$
Low-level convective available potential energy[a]	$\text{CAPE}_l = \overline{\text{CAPE}} + R[\theta'_{eb} - a'_0(\theta'_1 + \gamma'_2 \theta'_2)]$
Convective available potential energy at RCE	$\overline{\text{CAPE}} = H_m^2 \overline{Q}^2$
Radiative Cooling	$\mathcal{S}_j^{\theta} = -Q_{R,j} - \frac{1}{\tau_D} \theta_j, \ j = 1, 2$
Precipitation rate	$\mathcal{P} = \frac{2\sqrt{2}}{\pi} H_d$
Moisture source	$\mathcal{S}^q = \delta E \Delta_t \theta_e + \left(\delta M_d + \frac{\partial v_0}{\partial y} \right) \Delta_m \theta_e$
Surface turbulent moist thermodynamic fluxes ($\phi = \theta, \theta_e$)	$\frac{1}{\delta \pi} \langle w' \phi' \rangle_s = \frac{1}{\tau_e} (\phi_s - \phi_b)$
Surface momentum turbulent drag	$\frac{1}{\delta \pi} \langle w' \boldsymbol{u}' \rangle_s = -C_d U \boldsymbol{u}_b.$
Moist thermodynamic turbulent entrainment ($\phi = \theta, \theta_e$)	$\frac{1}{\delta \pi} \langle w' \phi' \rangle_t = M_u (\phi_b - \phi_t) - M_d (\phi_m - \phi_t)$
Momentum turbulent entrainment	$\frac{1}{\delta \pi} \langle w' \boldsymbol{u}' \rangle_t = \frac{1}{\tau_T} (\boldsymbol{u}_b - \boldsymbol{u}_t)$
Total downdraft mass flux	$M_d = \left\{ D_c + \frac{\partial v_b}{\partial y} \right\}^+$
Convective updraft mass flux	$M_u = \frac{1}{\alpha_m} D_c$
Mass flux velocity from large-scale and convective downdrafts	$D_c = m_0 \left\{ 1 + \frac{\mu}{Q_{R1}} (H_s - H_c) \right\}^+$
Moist thermodynamic turbulent entrainment velocity at top of ABL	$E = \left(M_u - M_d + \frac{\partial v_b}{\partial y} \right)^+$
Momentum turbulent entrainment velocity at top of ABL	$E_u = \left(\frac{1}{\tau_T} + \frac{\partial v_b}{\partial y} \right)^+$
Boundary layer radiative cooling ($\phi = \theta, \theta_e$)	$\langle \mathcal{S}^{\phi} \rangle = -Q_{Rb}$

[a] The primes in the associated equations indicate deviations for the radiative convective equilibrium (RCE) solution

$$
\begin{aligned}
&\frac{D_0 v_2}{Dt} + v_2 \frac{\partial v_0}{\partial y} + \left(\frac{\mathbf{2}}{\mathbf{3}} \boldsymbol{v_1} - \frac{\mathbf{1}}{\mathbf{2}} \boldsymbol{v_2} \right) \frac{\boldsymbol{\partial v_0}}{\boldsymbol{\partial y}} + y u_2 = \frac{\partial \theta_2}{\partial y} + \mathcal{S}_2^v, \\
&\frac{D_0 \theta_2}{Dt} + \frac{\sqrt{2}}{4} \left(v_1 \frac{\partial \theta_1}{\partial y} - \theta_1 \frac{\partial v_1}{\partial y} \right) - \frac{1}{4} \frac{\partial v_2}{\partial y} + \frac{\mathbf{1}}{\mathbf{2}} \left(\frac{\mathbf{4}}{\mathbf{3}} \boldsymbol{\theta_1} + \boldsymbol{\theta_2} \right) \frac{\boldsymbol{\partial v_0}}{\boldsymbol{\partial y}} + \frac{\boldsymbol{\sqrt{2}}}{\mathbf{4}} \frac{\boldsymbol{\partial v_0}}{\boldsymbol{\partial y}} = \frac{1}{2} \mathcal{H}_2^{\theta} + \frac{1}{2} \mathcal{S}_2^{\theta}.
\end{aligned}
\tag{11}
$$

The shorthand notation $(D_0/Dt) = (\partial/\partial t) + v_0(\partial/\partial y)$ is the barotropic transport operator. The nonzero horizontal divergence of the barotropic wind, Eq. (10), leads to linear and nonlinear contributions to the basic equations of motion (11), which are evidenced in bold.

The right-hand terms $\mathcal{S}_j^{u,v,\theta}$, $\mathcal{H}_j^{\theta}$ represent the radiative, convective, and turbulent forcing, respectively. For simplicity in exposition and streamlining, these are listed in Table 2 with the associated parameters listed in Table 3, following earlier work [29,61]. We note that some parameters are not specified in Table 3 but bear the mention "determined at RCE." An RCE is short for a radiative convective equilibrium, which is essentially a space and time homogeneous solution to the model equations. Without constraints, the model equations admit multiple equilibria. To construct a physical RCE solution, we fix a few key variables to their observed climatological values and use the RCE equations to constrain the remaining variables. Details of this procedure can be found in earlier publications [8,29,61].

Table 3 Multicloud and ABL model parameters

Parameter	Value (in dimensional units)	Description
H_m	5 km	Average height of the middle troposphere
R	320 J kg^{-1} K^{-1}	CAPE constant
Q_{R1}	1 K/day	Longwave first baroclinic radiative cooling rate
Q_{R2}	Determined at RCE	Longwave second baroclinic radiative cooling rate
$\overline{Q}$	Determined at RCE	Heating potential at RCE
m_0	Determined at RCE	Downdraft velocity reference scale
τ_c^0	2 h	Reference convective timescale
α_c, α_s	0.25, 0.25	Contribution of CAPE to congestus, stratiform heating
a_0	1 or 3	Contribution of θ_1 to deep convective heating anomalies
a_1	0.45	Contribution of θ_{eb} to deep convective heating anomalies
a_2	$1 - a_1$	Contribution of q to deep convective heating anomalies
a_0'	1.7	Contribution of θ_1 to CAPE anomalies
γ_2	0.1	Relative contribution of θ_2 to deep convective anomalies
γ_2'	2.0	Relative contribution of θ_2 to low-level CAPE anomalies
CAPE$_0$	200 J kg^{-1}	Reference value of CAPE
T_0	10 K	Reference value of CAPE
α_2	0.1	Relative contribution of θ_2 to θ_{em}
μ	0.25	Contribution of convective downdrafts to M_d
τ_c, τ_s	1 h, 3 h	Congestus, stratiform adjustment timescales
τ_{conv}	2 h	Convective timescale
θ^-, θ^+	10 K, 20 K	Moisture switch threshold values
τ_D	50 days	Newtonian cooling timescale
τ_R	75 days	Rayleigh drag timescale
τ_T	8 h	Momentum entrainment timescale
h_b	500 m	ABL depth
τ_e	Determined at RCE, of $\mathcal{O}$(7 h)	Surface evaporation timescale
U	2 m/s	Strength of turbulent velocity
C_d	0.001	Surface drag coefficient
τ_T	8 h	Momentum entrainment timescale
Q_{R_b}	Determined at RCE, of $\mathcal{O}$(5 K/day)	ABL radiative cooling rate
δ	0.03125	Ratio of boundary layer depth to height of the troposphere
α_m	0.2	Ratio of D_c to M_u

The free troposphere dynamics is coupled to the moisture equation (conservation of water vapor) through the processes of precipitation and latent heat release. Following [29,61], the troposphere moist dynamics has a background moisture profile that is exponentially decaying in the vertical, and the perturbation from this background is vertically averaged over the free troposphere depth which yields the bulk moisture equation, in nondimensional form:

$$\frac{D_0 q}{Dt} + \frac{\partial}{\partial y}\left((\tilde{\alpha}_1 v_1 + \tilde{\alpha}_2 v_2)q + \tilde{Q}_1 v_1 + \tilde{Q}_2 v_2 - \tilde{Q}_0 v_0\right) \boldsymbol{-\kappa q \frac{\partial v_0}{\partial y}} = -\mathcal{P} + \mathcal{S}^q. \tag{12}$$

The detailed form of the precipitation rate $\mathcal{P}$ and moisture source $\mathcal{S}^q$, due to turbulent mixing and evaporation, is also given in Table 2. The details of the derivation of the bulk moisture equation can be found in [8] and [29]. Here, following [8], we use the nondimensional parameter/constant values $\tilde{Q}_0 = 1.674$, $\tilde{Q}_1 = 0.559$, $\tilde{Q}_2 = 0.209$, $\tilde{\alpha}_1 = 1$, $\tilde{\alpha}_2 = 0.1$, and $\kappa = 2$.

The ABL is assumed to be well mixed at all times such that no stratification is allowed to settle. It is represented by a Reynolds-averaged hydrostatic Boussinesq fluid on the β-plane with horizontal velocity $\boldsymbol{u} = (u, v)$, fluctuation potential temperature θ, and equivalent potential temperature θ_e. Since the ABL is effectively homogenized by turbulence, a bulk description, following the approach of Stevens [59] (see also [61]), is a justifiable approximation. The bulk model consists of integrating out the vertical dependencies to represent the bulk dynamic and thermodynamic structure of the ABL.

Following [59,61], we assume the Reynolds decomposition [22] of the flow variables in the form $\phi = \langle\phi\rangle + \phi'$, where $\langle\phi\rangle$ represents the (slowly evolving) resolved scales and ϕ' represents the unresolved turbulent fluctuations. Here ϕ is a generic scalar field. Defining ϕ_b to be the vertical average of $\langle\phi\rangle$ over the ABL of nondimensional depth $\delta\pi$, $\phi_b = \frac{1}{\delta\pi}\int_{-\delta\pi}^{0}\langle\phi\rangle \mathrm{d}z$, it is straightforward (see [8]) to show that the zonally averaged dimensionless equations for the ABL are [61]:

$$\frac{\partial u_b}{\partial t} + \frac{\partial (v_b u_b)}{\partial y} + \frac{1}{\delta\pi}\langle w\rangle_t \langle u\rangle_t - y v_b = -\frac{1}{\delta\pi}\langle u'w'\rangle_t + \frac{1}{\delta\pi}\langle u'w'\rangle_s, \tag{13a}$$

$$\frac{\partial v_b}{\partial t} + \frac{\partial \left(v_b^2\right)}{\partial y} + \frac{1}{\delta\pi}\langle w\rangle_t \langle v\rangle_t + y u_b = -\frac{\partial p_b}{\partial y} - \frac{1}{\delta\pi}\langle v'w'\rangle_t + \frac{1}{\delta\pi}\langle v'w'\rangle_s, \tag{13b}$$

$$\frac{\partial \theta_b}{\partial t} + \frac{\partial (v_b \theta_b)}{\partial y} + \frac{1}{\delta\pi}\langle w\rangle_t \langle \theta\rangle_t = -\frac{1}{\delta\pi}\langle \theta'w'\rangle_t + \frac{1}{\delta\pi}\langle \theta'w'\rangle_s + \langle \mathcal{S}^{\theta}\rangle, \tag{13c}$$

$$\frac{\partial \theta_{eb}}{\partial t} + \frac{\partial (v_b \theta_{eb})}{\partial y} + \frac{1}{\delta\pi}\langle w\rangle_t \langle \theta_e\rangle_t = -\frac{1}{\delta\pi}\langle \theta_e'w'\rangle_t + \frac{1}{\delta\pi}\langle \theta_e'w'\rangle_s + \langle \mathcal{S}^{\theta_e}\rangle. \tag{13d}$$

Here we used the rigid lid boundary condition at the surface (4), the divergence relation to write the equations in flux form, and the following approximation from [59]:

$$\frac{1}{\delta\pi}\int_{-\delta\pi}^{0} \langle v\rangle\langle\phi\rangle \, \mathrm{d}z \approx v_b \phi_b.$$

The new terms $\langle u'w'\rangle$ and $\langle v'w'\rangle$ are vertical turbulent fluxes of horizontal momentum, whereas $\langle \theta'w'\rangle$ and $\langle \theta_e'w'\rangle$ are vertical turbulent heat and moisture fluxes. The subscripts s and t denote evaluations at the Earth's surface $z = -\delta\pi$, and at the top $z = 0$ of the ABL, respectively. The terms $\mathcal{S}^{\theta}$ and $\mathcal{S}^{\theta_e}$ are source terms for the ABL potential and equivalent potential temperatures, respectively. Vertical averaging of the incompressibility and hydrostatic equations over the ABL depth gives [8,61]

$$\begin{aligned} w_t &= -\delta\pi \frac{\partial v_b}{\partial y}, \\ p_t &= p_s + \delta\pi\theta_b. \end{aligned} \tag{14}$$

The former was obtained using the rigid lid condition (4). Moreover, the pressure and vertical velocity fields, in the ABL, are assumed to have the linear profiles (see Fig. 2) [61],

$$w(z) = -(z+\delta\pi)\frac{\partial v_b}{\partial y}, \quad -\delta\pi \le z \le 0, \tag{15}$$

$$p(z) = p_s + (z+\delta\pi)\theta_b, \quad -\delta\pi \le z \le 0, \tag{16}$$

and a vertical average of the last equation yields the bulk ABL pressure in terms of the bulk potential temperature,

$$p_b = p_s + \frac{\delta\pi}{2}\theta_b, \quad -\delta\pi \le z \le 0. \tag{17}$$

The turbulent fluxes are closed through simple aerodynamics formulas [59,61] and are summarized in Table 2, for convenience.

With the closures in Table 2 and the above simplifications, the ABL bulk equations read

$$\frac{D_b \theta_{eb}}{Dt} = -E\Delta_t\theta_e - M_d\Delta_m\theta_e + \frac{1}{\tau_e}\Delta_s\theta_e - Q_{Rb} \tag{18a}$$

$$\frac{D_b \theta_b}{Dt} = -E\Delta_t\theta - M_d\Delta_m\theta + \frac{1}{\tau_e}\Delta_s\theta - Q_{Rb} \tag{18b}$$

$$\frac{D_b u_b}{Dt} - y v_b = -E_u\Delta_t u - C_d U u_b \tag{18c}$$

$$\frac{D_b v_b}{Dt} + y u_b = -\frac{\partial p_b}{\partial y} - E_u\Delta_t v - C_d U v_b \tag{18d}$$

Here $(D_b/Dt) = (\partial/\partial t) + v_b(\partial/\partial y)$ is the meridional boundary layer transport operator, while the newly introduced forcing terms are defined in Table 2. The scalar and momentum differences between two heights were conveniently written as downward gradients. We have,

$$\Delta_s\phi \equiv \phi_s - \phi_b, \quad \Delta_t\phi \equiv \phi_b - \phi_t, \quad \Delta_m\phi \equiv \phi_b - \phi_m, \tag{19}$$

for a scalar ϕ. The ABL parameter values are listed in Table 3.

2.2 The Poisson equation for pressure

We now derive the Poisson equation for barotropic and ABL pressure. In the three vertical mode framework, the free tropospheric pressure satisfies $p = p_0 + p_1 C_1 + p_2 C_2$, where C_1 and C_2 are the cosine basis functions defined above, and p_0, p_1 and p_2 are the pressure wave amplitudes of modes 0, 1, and 2. While the first and second baroclinic pressure components relate directly to the baroclinic potential temperatures according to (8), the barotropic pressure p_0 is left to be determined, along with the ABL bulk pressure p_b.

Assuming continuity of pressure across the interface between the free troposphere and the ABL, we must require that $\lim_{z\to 0^+} p(y,z,t) \equiv p_t$, where $p_t = p_b + \delta\pi\theta_b/2$ is found from (17). We then have the following relation between the barotropic and ABL pressures:

$$p_0 = p_b + \frac{\delta\pi}{2}\theta_b + \sqrt{2}\,(\theta_1 + \theta_2)\,, \tag{20}$$

where the baroclinic hydrostatic relations (8) were used. A governing equation for the ABL pressure is found by taking the divergence of both the barotropic and ABL meridional momentum equations and using the divergence relation (10) together with relation (20). We have:

$$\frac{\partial^2 p_b}{\partial y^2} = \frac{1}{\delta+1}\left(\frac{\partial \Phi}{\partial y} - \frac{\partial^2 \phi}{\partial y^2}\right) \tag{21a}$$

$$\Phi = \sqrt{2}(v_1 + v_2)\frac{\partial v_0}{\partial y} - y(u_0 + \delta u_b) - \delta E_u \Delta_t v - \delta C_d U v_b + \mathcal{S}_0^v, \tag{21b}$$

$$\phi = \frac{\delta}{2}{v_b}^2 + \frac{1}{2}{v_0}^2 + {v_1}^2 + {v_2}^2 + \frac{\delta\pi}{2}\theta_b + \sqrt{2}(\theta_1 + \theta_2). \tag{21c}$$

In practice, we solve only for the pressure gradient $\partial p_b/\partial y$ through a straightforward integration starting at the southern boundary point, enforcing a Neumann boundary condition $\partial(\cdot)/\partial y = 0$ on both ends for all pressure and potential temperature components.

2.3 The stochastic multicloud parameterization for subgrid scale cloud processes

The stochastic multicloud model is introduced in [27] to represent the unresolved variability due to organized tropical convection in GCMs. The motivation for the use of a stochastic model in a GCM is at least twofold. Firstly, it introduces significant background noise for the model simulation and increases the likelihood of the ensemble average to be closer to the true climate state, i.e., the stochasticity is regarded as representative of the model error [52] and secondly, as in this case, it can be targeted to mimic the variability of some particular unresolved process without significant computational overhead [13,27,44,55]. The SMCM is based on a Markov chain lattice model that mimics small-scale convective elements, which interact with each other and with the large-scale environment according to a set of probability rules. It is assumed to represent the unresolved dynamics of the three cloud types that are observed to characterize tropical convective system building blocks and to set the heating and cooling profiles of the tropical atmosphere, namely cumulus congestus cloud decks that heat the lower troposphere and cool the upper troposphere, deep convective towers that heat the entire troposphere, and stratiform anvils that warm and dry the upper troposphere and cool and moisten the lower troposphere. Our meridional (South–North) domain is thus meshed into uniform gridboxes of about 100 km each. Each gridbox is associated with a rectangular lattice of $n \times n$ sites. The parameter n is a positive integer of $\mathcal{O}(100)$, so that the lattice sites have horizontal extent of about 1 kilometer. The multicloud model associates with each lattice site i a four-state stochastic Markov process $(Y_t^i)_{t>0}$ taking the values 0, 1, 2, or 3, depending on whether it is clear sky, or occupied by a congestus, deep, or stratiform cloud, respectively. A given site will switch from its current cloud configuration to another according to transition probabilities, which depend on the large-scale resolved variables. In the simple case where local interactions are ignored, all n^2 stochastic processes $(Y_t^i)_{t>0}$ are independent and identically distributed [27], and the probability rules depend only on the large-scale resolved variables. These large-scale variables are the scaled convective available potential energy (CAPE, a measure of atmospheric instability to moist convection) integrated over the whole troposphere (C) and over the lower troposphere (C_l),

$$C = \frac{\text{CAPE}}{\text{CAPE}_0} \quad \text{and} \quad C_l = \frac{\text{CAPE}_l}{\text{CAPE}_0},$$

Table 4 Rates r_{jk} and timescales τ_{jk} of the cloud transitions in the multicloud model

Cloud transition	Probability rate	Timescale (h)
Formation of congestus	$r_{01} = \frac{1}{\tau_{01}} \Gamma(C_l)\Gamma(D)$	$\tau_{01} = 31.789$
Decay of congestus	$r_{10} = \frac{1}{\tau_{10}} \Gamma(D)$	$\tau_{10} = 1.761$
Conversion of congestus to deep	$r_{12} = \frac{1}{\tau_{12}} \Gamma(C)\big(1 - \Gamma(D)\big)$	$\tau_{12} = 0.238$
Formation of deep	$r_{02} = \frac{1}{\tau_{02}} \Gamma(C)\big(1 - \Gamma(D)\big)$	$\tau_{02} = 11.821$
Conversion of deep to stratiform	$r_{23} = \frac{1}{\tau_{23}}$	$\tau_{23} = 0.257$
Decay of deep	$r_{20} = \frac{1}{\tau_{20}} \big(1 - \Gamma(C)\big)$	$\tau_{20} = 9.552$
Decay of stratiform	$r_{30} = \frac{1}{\tau_{30}}$	$\tau_{30} = 1.021$

The transition rates r_{jk} are functions of the large-scale variables CAPE (C), low-level CAPE (C_l), and mid-troposphere dryness D, via the activation function Γ defined in (22). The transition timescales are obtained from cloud simulation data based on a Bayesian inference technique [9,10]

and the mid-troposphere dryness (D) defined as

$$D = \frac{\theta_{eb} - \theta_{em}}{T_0}, \quad \text{where} \quad \theta_{em} \approx \frac{2\sqrt{2}}{\pi}(\theta_1 + \alpha_2\theta_2) + q.$$

Here CAPE_0 and T_0 are (nondimensional) reference values for CAPE and dryness, respectively. The interaction rules between the different cloud types and the environment, which are designed in accordance with observations of cloud dynamics in the tropics, are summarized as follows [27]:

1. A clear site turns into a congestus site with high probability if low-level CAPE is positive and the middle troposphere is dry;
2. A congestus or clear sky turns into a deep convective site with high probability if CAPE is positive and the middle troposphere is moist;
3. A deep convective site turns into a stratiform site with high probability;
4. All three cloud types decay naturally to clear sky at some fixed rate;
5. All other transitions are assumed to have negligible probability.

These rules are formalized by the probability transition rates r_{kl} listed in Table 4, in terms of the Arrhenius-type activation function

$$\Gamma(x) = \left\{1 - e^{-x} \text{ if } x > 0,\ 0 \text{ otherwise}\right\}, \tag{22}$$

and a set of cloud transition timescale parameters τ_{kl}. Note that from Assumption 5, we have $r_{03} = r_{13} = r_{21} = r_{31} = r_{32} = 0$.

In practice, evolving in time each one of the $N = n^2$ microscopic Markov chains has a high computational overhead. Since the chains are independent, however, a coarse-graining technique is easily applied, leading to the stochastic dynamics of the GCM gridbox cloud coverages alone, without the detailed knowledge of the microstate configuration [24,33]. The cloud coverages or area fractions σ_c, σ_d, and σ_s occupied by clouds of type congestus, deep, or stratiform are given by

$$\sigma_c^t = \frac{1}{N}\sum_{i=1}^{N} \mathbb{1}_{\{Y_t^i=1\}}, \quad \sigma_d^t = \frac{1}{N}\sum_{i=1}^{N} \mathbb{1}_{\{Y_t^i=2\}}, \quad \sigma_s^t = \frac{1}{N}\sum_{i=1}^{N} \mathbb{1}_{\{Y_t^i=3\}}, \tag{23}$$

where $\mathbb{1}_{\{Y_t^i=k\}}$ is the indicator function, which takes the value one if $Y_t^i = k$ and zero otherwise.

As a function of time, the triplet $(\sigma_c^t, \sigma_d^t, \sigma_s^t)$ is effectively a three-dimensional birth–death-like process with probability transition rules that are given in terms of the microscopic rates r_{kl}. Given the large-scale thermodynamic state, the birth–death process is easily evolved in time using Gillespie's exact algorithm [6,18,27] and yields the dynamical evolution of the cloud fractions σ_c, σ_d, and σ_s.

The SMCM is feedbacked onto the free troposphere dynamic equations in (11) by modulating the heating and cooling rates. Following [30], the first baroclinic mode is forced by deep convection, and the second

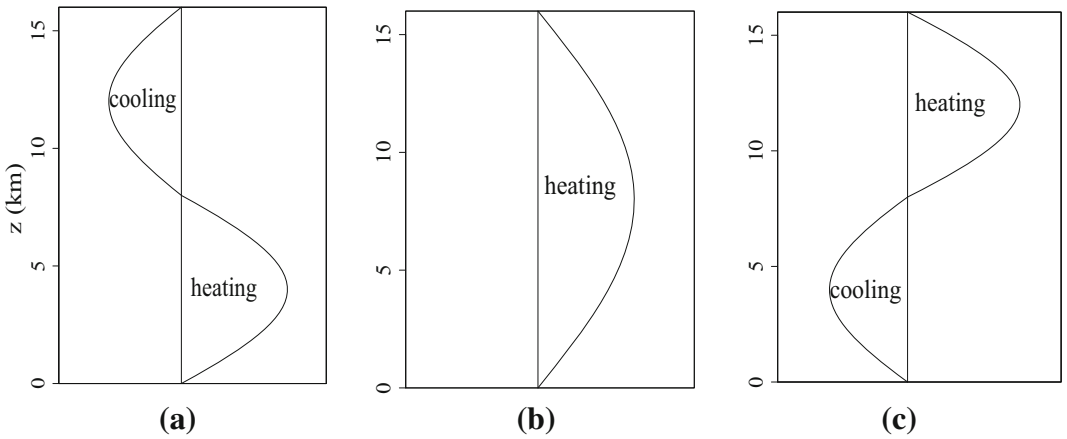

Fig. 3 Vertical profiles of heating and cooling fields associated with the three cloud types of the multicloud model. The deep heating vertical profile has the half-sine structure of S_1, whereas the congestus and stratiform have the full-sine structure of S_2. The heating curves intersect the *vertical straight lines* at zero heating points. **a** Congestus. **b** Deep. **c** Stratiform

baroclinic mode is forced by both congestus and stratiform clouds, as depicted in Fig. 3. Therefore, the Markov model discussed here and the dynamical core large-scale model presented in the previous subsection interact both ways and form a closed system. The large-scale model provides the convective predictors, namely CAPE and mid-tropospheric moisture, which change the stochastic transition rates as defined in Table 4, while the stochastic Markov model provides the area fractions which modulate the associated heating rates as defined in Table 2.

The heating rates H_c, H_d, and H_s associated with the three cloud types are assumed to be proportional to the area coverages σ_c, σ_d, and σ_s and are closed in terms of the large-scale variables as summarized in Table 2.

3 Numerical strategy and validation

The eight free tropospheric equations in (11), the mid-tropospheric moisture equation in (12), the bulk ABL equations (18) coupled to the elliptic equation for pressure (21), the closure equations in Table 2 supplemented with the stochastic multicloud parameterization presented in Sect. 2.3, and the parameter values defined in Table 3 form the full zonally symmetric model for the tropical meridional circulation with stochastic convective forcing. It is a highly nonlinear and nonconservative system of PDEs. Here, we focus on the dynamical core, i.e., the equations of motion in (11) and (18), together with the mid-tropospheric moisture equation (12) and the equation for pressure (21), without the forcing terms on the right-hand side, putting aside the stochastic convection parameterization in particular. This is still a fairly large set of PDEs coupled through the advection nonlinearities. We present now a numerical method for this system and its validation using an artificial exact solution with the expected second-order convergence under grid refinement. Our strategy is based on the time operator splitting of Strang [60], where the nonconservative system is judiciously divided into a conservative part, a hyperbolic part, and a nilpotent part, following an idea put forward in [28] and used in [57]. The three parts are handled separately by the nonoscillatory central scheme of Nessyahu and Tadmor [50] (NT below; see also [23]), the wave propagation method of LeVeque [41], and the method of lines, respectively.

3.1 Numerical discretization of the nonconservative system

We start by writing the coupled system formed by (11), (12) and (18) as

$$\frac{\partial \boldsymbol{\xi}}{\partial t} + \frac{\partial \boldsymbol{F}(\boldsymbol{\xi}, p_b)}{\partial y} + D_{nc}(\boldsymbol{\xi})\frac{\partial \boldsymbol{\xi}}{\partial y} + N_{nc}(\boldsymbol{\xi})\frac{\partial \boldsymbol{\xi}}{\partial y} = \boldsymbol{S}(\boldsymbol{\xi}), \tag{24}$$

Here, $\boldsymbol{\xi}(y,t) : \mathbb{R} \times \mathbb{R} \to \mathbb{R}^{13}$ is a vector field representing the 13 unknown prognostic variables (winds, temperature, and moisture), $\boldsymbol{F}(\boldsymbol{\xi}, p_b) : \mathbb{R}^{13} \times \mathbb{R} \to \mathbb{R}^{13}$ is a flux vector, $D_{nc} \in \mathbb{R}^{13\times 13}$ is a diagonal matrix, and $N_{nc} \in \mathbb{R}^{13\times 13}$ is a matrix of nilpotency 4. These are listed in Table 5 for the sake of completeness. As

Table 5 Components of the split nonconservative system for zonally symmetric tropical circulation

$$\boldsymbol{\xi} = \begin{pmatrix} \theta_{eb} \\ \theta_b \\ u_b \\ v_b \\ u_0 \\ v_0 \\ u_1 \\ v_1 \\ u_2 \\ v_2 \\ \theta_1 \\ \theta_2 \\ q \end{pmatrix}, \quad \boldsymbol{F}(\boldsymbol{\xi}, p_b) = \begin{pmatrix} 0 \\ 0 \\ 0 \\ v_b^2/2 + p_b \\ u_1 v_1 + u_2 v_2 \\ v_0^2/2 + v_1^2 + v_2^2 + p_b + \delta\pi\theta_b/2 + \sqrt{2}(\theta_1 + \theta_2) \\ \sqrt{2}u_2 v_1/2 \\ -\theta_1 \\ \sqrt{2}u_1 v_1/2 \\ -\theta_2 \\ \sqrt{2}v_1\theta_2 - v_1 + \sqrt{2}v_0 \\ \sqrt{2}v_1\theta_1/4 - v_2/4 + \sqrt{2}v_0/4 \\ (\tilde{\alpha}_1 v_1 + \tilde{\alpha}_2 v_2)q + \tilde{Q}_1 v_1 + \tilde{Q}_2 v_2 - \tilde{Q}_0 v_0 \end{pmatrix}, \quad D_{nc}(\boldsymbol{\xi}) = \operatorname{diag} \begin{pmatrix} v_b \\ v_b \\ v_b \\ 0 \\ v_0 \\ -\sqrt{2}(v_1 + v_2) \\ v_0 + \sqrt{2}v_2/2 \\ v_0 + 3\sqrt{2}v_2/2 \\ v_0 \\ v_0 \\ v_0 - \sqrt{2}v_2/2 \\ v_0 \\ v_0 \end{pmatrix}$$

$$N_{nc}(\boldsymbol{\xi}) = \begin{pmatrix} 0_{3\times4} & 0_{3\times6} & 0_{3\times3} \\ 0_{10\times4} & \tilde{N}_{nc}(\boldsymbol{\xi}) & 0_{10\times3} \end{pmatrix}, \quad \tilde{N}_{nc}(\boldsymbol{\xi}) = \begin{pmatrix} 0 & 0 & 0 & 0 & 0 & 0 \\ 0 & -\sqrt{2}(u_1 + u_2) & 0 & 0 & 0 & 0 \\ 0 & 0 & 0 & 0 & 0 & 0 \\ v_1 & -u_1/2 - 8u_2/3 & 0 & \sqrt{2}u_2/2 & 0 & \sqrt{2}u_1/4 \\ 0 & v_1/2 - 8v_2/3 & 0 & 0 & 0 & 3\sqrt{2}v_1/4 \\ v_2 & 2u_1/3 - u_2/2 & 0 & -\sqrt{2}u_1 & 0 & 0 \\ 0 & 2v_1/3 + v_2/2 & 0 & 0 & 0 & 0 \\ 0 & \theta_1/2 - 8\theta_2/3 & 0 & \sqrt{2}\theta_2 & 0 & -\sqrt{2}\theta_1/4 \\ 0 & 2\theta_1/3 + \theta_2/2 & 0 & -\sqrt{2}\theta_1/2 & 0 & 0 \\ 0 & -\kappa q & 0 & 0 & 0 & 0 \end{pmatrix}$$

pointed out earlier, the barotropic divergence relationship (10), $\partial v_0/\partial y = -\delta \partial v_b/\partial y$, is enforced through the one-dimensional elliptic equation for pressure (21). Since the equation for the barotropic meridional wind is also enforced through (21a), it may be eliminated from (24) and v_0 is calculated from v_b using the low-cost divergence relation (10). The forcing term $\mathbf{S}(\boldsymbol{\xi})$ in (24) contains the remaining right-hand terms of (11), (12), and (18), and the associated Coriolis forcing terms.

The choice of the split form (24) is preferred over various other mathematical forms because of the system's important following properties:

1. It has a nonlinear conservative part, that is, terms that can be arranged as

$$\frac{\partial \boldsymbol{\xi}}{\partial t} + \frac{\partial \boldsymbol{F}(\boldsymbol{\xi}, p_b)}{\partial y} = 0, \qquad \frac{\partial \boldsymbol{F}}{\partial \boldsymbol{\xi}} := A_c(\boldsymbol{\xi}), \tag{25a}$$

   where the flux function $\boldsymbol{F}$ is a nonlinear function of $\boldsymbol{\xi}$, and A_c is the flux Jacobian matrix. Since the matrix of wave propagation speeds A_c depends on the solution $\boldsymbol{\xi}$, spontaneous discontinuities in the solution may develop from smooth initial data. The eigenstructure of A_c is not accessible analytically, and thus, regions of hyperbolicity of the system for physically relevant values of p_b are not known. In the nonhyperbolic regime, the solution can develop instabilities (see [57]).
2. It has a nonconservative nonlinear hyperbolic part which takes the form

$$\frac{\partial \boldsymbol{\xi}}{\partial t} + D_{nc}(\boldsymbol{\xi}) \frac{\partial \boldsymbol{\xi}}{\partial y} = 0, \tag{25b}$$

   where D_{nc} is a diagonal matrix which depends on the solution $\boldsymbol{\xi}$.
3. It has a nonconservative nonlinear advection system of the form

$$\frac{\partial \boldsymbol{\xi}}{\partial t} + N_{nc}(\boldsymbol{\xi}) \frac{\partial \boldsymbol{\xi}}{\partial y} = 0, \tag{25c}$$

   where N_{nc} was chosen so that all its eigenvalues (linear wave speeds) are zero. In particular, N_{nc} has a nilpotency degree 4 ($N_{nc}^4 = 0$).

The list above highlights mathematical properties that need to be considered when designing a numerical method for the nonconservative PDE system (24). It presents the system as a combination of three subproblems (four with the forcing term $\boldsymbol{S}$), each of which is discretized separately using its own proper method.

The subproblem (25a) is the conservative part of the system and is tied to the evaluation of the pressure. Here we use the second-order nonoscillatory NT scheme, despite the fact that (25a) is (for constant pressure) at most only conditionally hyperbolic. The pressure is diagnosed simultaneously with the NT scheme by solving the one-dimensional elliptic equation (21) at every time step. We can expect a degradation of the method's accuracy and even possible instabilities occurring when the system falls into a nonhyperbolic regime. A careful analysis of the system's hyperbolic/nonhyperbolic regions of the state space is beyond the scope of this paper. However, Stechmann et al. have demonstrated with numerical experiments, for the case of the two baroclinic modes alone, that the corresponding numerical scheme remains stable even when the solution is driven to regions of nonhyperbolicity [57].

For the nonlinear hyperbolic part of the system, we use the wave propagation method of [42] with a linearized Riemann solver. Although the method gives second-order accuracy when applied to quasilinear hyperbolic problems with a constant coefficient matrix, formal second-order accuracy is not granted when used on variable-coefficient problems of the form (25b) [40].

Finally, the method of lines [42] is used to solve the nonconservative subproblem (25c). The method of lines reduces the initial PDE system (25c) into a system of ODEs after using centered finite differences on the spatial derivatives. We solve the resulting system in time using conventional ODE solvers where a second-order Runge–Kutta scheme is used to advance in time. It remains to solve the pressure gradient. Integrating (21a) once readily gives

$$\frac{\partial p_b}{\partial y} = C + \frac{1}{1+\delta}\left[\Phi - \Phi|_{y=a} - \frac{\partial \phi}{\partial y} + \frac{\partial \phi}{\partial y}\bigg|_{y=a}\right], \quad y \in [a, b], \tag{26}$$

Where C is the integration constant. The pressure gradient, which arises naturally as a forcing term in the momentum equations, is thus determined up to an arbitrary additive constant by this method. The choice here for that constant is $C = \partial p_b/\partial y|_{y=a} = 0$, which is obtained by setting $y = a$ in (26). This in turn constrains the barotropic pressure gradient and ABL/baroclinic temperature gradients via the relationship (20):

$$\frac{\partial p_b}{\partial y} = \frac{\partial p_0}{\partial y} + \frac{\delta\pi}{2}\frac{\partial \theta_b}{\partial y} + \sqrt{2}\frac{\partial}{\partial y}(\theta_1 + \theta_2) = 0 \quad \text{at} \quad y = a, b. \tag{27}$$

This is automatically satisfied for the case of Neumann boundary condition imposed here:

$$\frac{\partial p_b}{\partial y} = \frac{\partial p_0}{\partial y} = \frac{\partial \theta_b}{\partial y} = \frac{\partial \theta_1}{\partial y} = \frac{\partial \theta_2}{\partial y} = 0 \quad \text{at} \quad y = a, b. \tag{28}$$

This corresponds to a situation where the fluid is not driven out of the computational domain by a pressure gradient; we are interested in the case of pure Boussinesq buoyancy driven flows.

3.2 Validation and grid convergence error analysis

Although the true solution to the governing PDE is not known, we can monitor grid convergence toward a nontrivial exact solution by adding the appropriate forcing to the PDE. The necessary condition is that the solution be nontrivial, that is, that it has significant solution structure to exercise higher-derivative calculations [56]. To this end, we use a traveling sine wave solution on a 2π-periodic domain for each one of the components of $\boldsymbol{\xi}$:

$$\xi^m_{wav}(y, t) = \sin(y - t), \quad m = 1, \ldots, 13, \quad y \in [0, 2\pi], \quad t \geq 0. \tag{29}$$

Although this mathematically naive solution is unphysical, it allows to accomplish the code verification just as well as physically realistic solutions.

We verify the numerical scheme for the advection part of the PDE, which we denote $\mathcal{L}(\boldsymbol{\xi}) := \boldsymbol{\xi}_t + [\boldsymbol{F}(\boldsymbol{\xi}, p_b)]_y + N_{nc}(\boldsymbol{\xi})\boldsymbol{\xi}_y + D_{nc}(\boldsymbol{\xi})\boldsymbol{\xi}_y$. The vector $\boldsymbol{\xi}_{wav}$ of traveling wave solutions (29) will then satisfy the following "balanced" system

$$\mathcal{L}(\boldsymbol{\xi}) = \boldsymbol{\Psi} \tag{30}$$

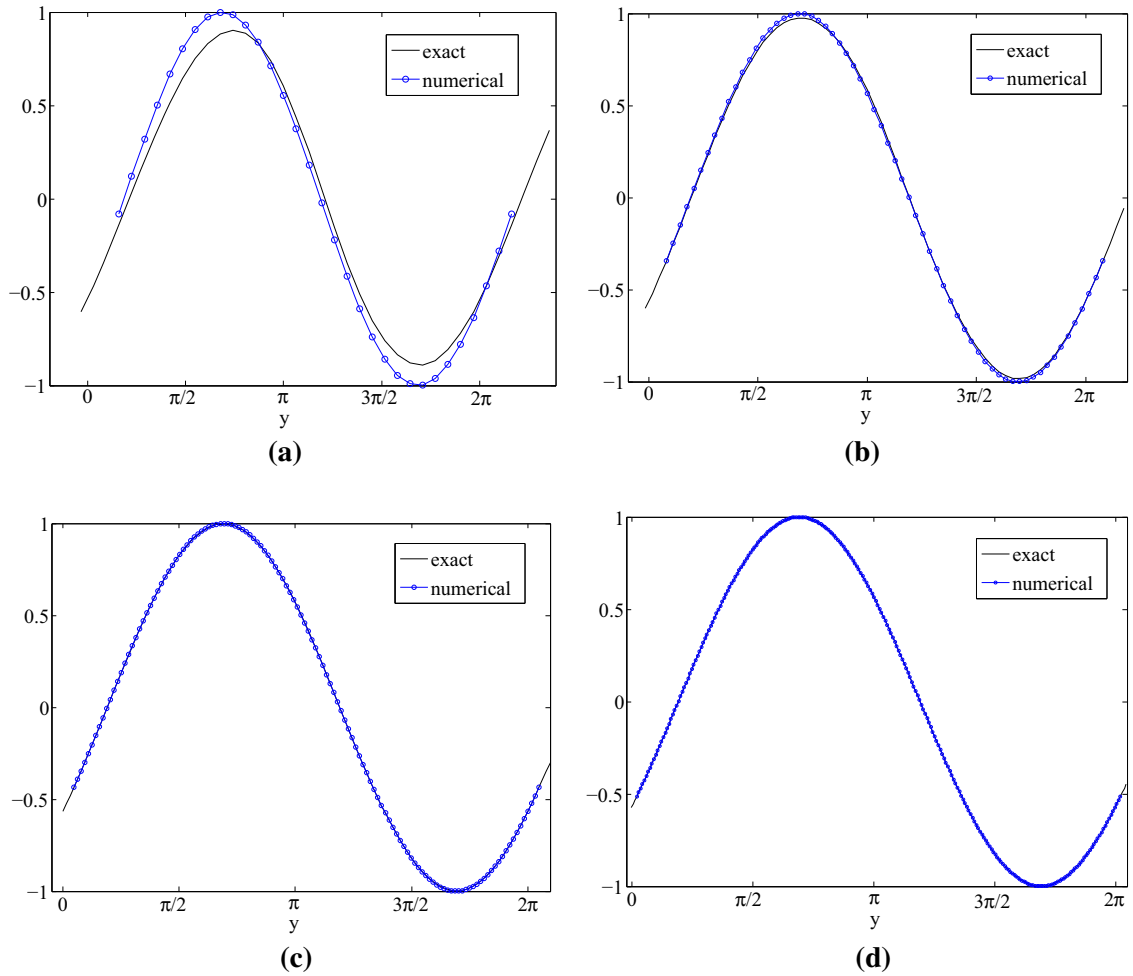

Fig. 4 Comparison of exact (*black*) and numerical (*blue*) solutions for the v_b sine wave (29) at $t = 0.6$ using a grid with 32, 64, 128, and 256 points. The time step is $\Delta t = \text{CFL}\Delta y/100$ with CFL $= 0.1$. **a** 32 grid points. **b** 64 grid points. **c** 128 grid points. **d** 256 grid points

exactly, where $\boldsymbol{\Psi} = \mathcal{L}(\boldsymbol{\xi}_{wav})$. In summary, the grid convergence test is carried on the following problem:

$$\begin{cases} \mathcal{L}(\boldsymbol{\xi}) = \boldsymbol{\Psi}, \quad y \in [0, 2\pi], \\ 2\pi - \text{periodic BC on } \boldsymbol{\xi} : \boldsymbol{\xi}(0) = \boldsymbol{\xi}(2\pi), \\ \dfrac{\partial^2 p_b}{\partial y^2} = \dfrac{1}{1+\delta}\left[\dfrac{\partial \Phi}{\partial y} - \dfrac{\partial^2 \phi}{\partial y^2}\right], \\ \text{BC on } \partial p_b/\partial y \\ \boldsymbol{\xi}(y, 0) = \boldsymbol{\xi}_{wav}(y, 0). \end{cases} \tag{31}$$

Note that Φ and ϕ are given by (21b) and (21c) except for the Coriolis and radiative convective forcing terms which are neglected. The ABL pressure gradient BC is merely a constant and is immaterial for the convergence results; it is set here to zero for simplicity, albeit inconsistent with periodic BC on the field variables. The system is solved using the Strang splitting strategy, with a trapezoidal second-order ODE solver for the forcing term.

A graphical comparison of the exact and numerical solutions is shown in Fig. 4 for the v_b variable using a grid with 32, 64, 128, and 256 points. The error between the exact and the numerical solutions is quantified at a fixed time for the m^{th} component of $\boldsymbol{\xi}$ using the 1-norm $\|e^m\|_1 = \Delta y \sum_{j=1}^{J} |\xi_j^m - \xi_{wav_j}^m|$, and the max-norm (or ∞-norm) $\|e^m\|_\infty = \max_{1\le j\le J} |\xi_j^m - \xi_{wav_j}^m|$, where J is the total number of grid points. Since the solution

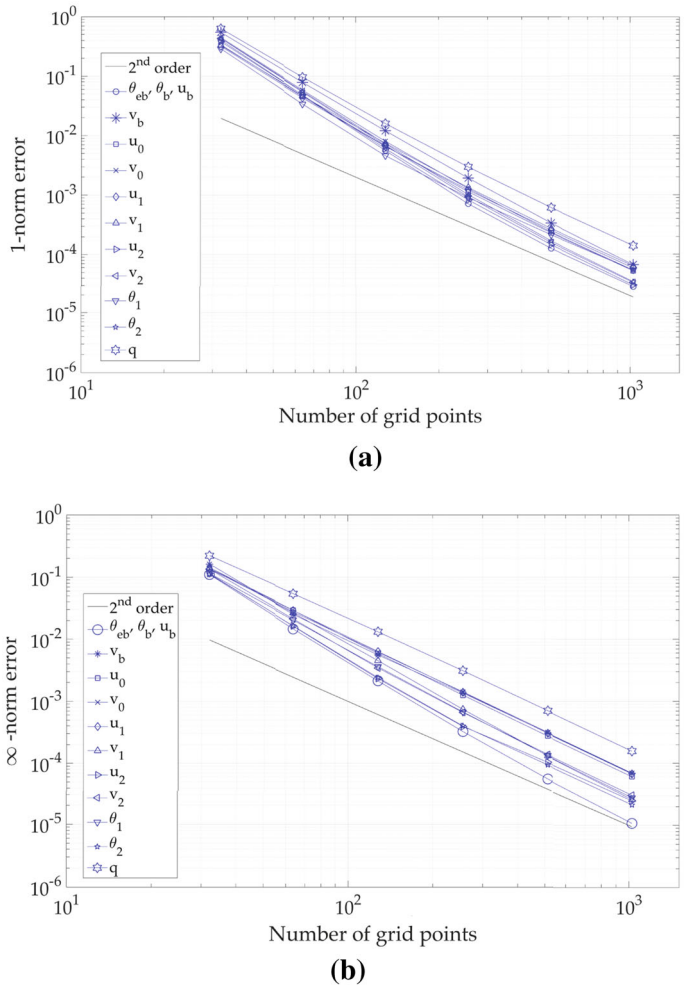

Fig. 5 Second-order convergence in the 1- and ∞-norm

$\boldsymbol{\xi}_{wav}$ is smooth, we expect pointwise convergence as measured by the max-norm. As expected, a second-order rate of convergence for all variables is demonstrated in Fig. 5a, b in both the 1-norm and max-norm, respectively.

4 Application to an idealized summer monsoon setting

In this section, we present simulation results of the dynamics of the Hadley-monsoon circulation and show that on an aquaplanet [2] with nonuniform sea-surface temperature (SST), realistic mean Hadley cells with monsoonal-type flow are reproduced with this simple model. More specifically, we integrate in time the fully-coupled free atmosphere-ABL numerical model forced by the radiative, convective, and turbulent source terms listed in Table 2 supplemented by the SMCM model for the cloud area fractions. The various parameters used here are listed in Table 3. The system is integrated as an initial value problem with the initial condition set to a radiative convective equilibrium (RCE) solution [29], i.e., a space and time homogeneous solution of the coupled model equations. The RCE value of CAPE is given by the solution of the nonlinear algebraic equation [27]

$$Q_{R1} = \frac{1}{H_m}\overline{\sigma_d}(\overline{\text{CAPE}})\sqrt{\overline{\text{CAPE}}},$$

where $\overline{\sigma_d}$ is the statistical RCE of the deep cloud coverage, defined as the equilibrium distribution [27] of the multistate Markov chain Y_t described in Sect. 2.3. For the stochastic part, the equilibrium values are given by the

limiting distribution of the ergodic Markov chain. Details on how to construct an RCE solution for the coupled system can be found in [8] (see also [26,27]). In the context of climate modeling, the computation of a realistic RCE solution is a useful exercise, which starts by imposing climatological values for air temperature and moisture profiles and constrain some unknown parameters such as the evaporative timescale or the reference scale for downdraft mass flux [29]. The RCE solution used here is based on temperature and moisture profiles, leading to the discrepancy values

$$\Delta_s\bar{\theta}_e = 10\text{K}, \Delta_s\bar{\theta} = 0, \Delta_t\bar{\theta}_e = 5\text{K}, \Delta_t\bar{\theta} = 0, \Delta_m\bar{\theta}_e = 11\text{K}, \Delta_m\bar{\theta} = -5.5\text{K},$$

where the overbars denote RCE values. These RCE values are not only based on realistic climatology, but they represent a stable equilibrium based on linear theory [8,29,61].

The system is forced by the uniform radiative cooling and by imposing a constant (in time) SST with a nonuniform meridional distribution on the form of a Gaussian centered at 15° N to mimic the location of the ITCZ during the Northern Hemisphere summer monsoon season. We note that for the model, this amounts to specifying the meridional distribution of $\Delta_s\bar{\theta}$ and $\Delta_s\bar{\theta}_e$ as shown in Fig. 6a for $\Delta_s\bar{\theta}_e$. The computational domain is reduced to a meridional slice of the troposphere between 40° S and 40° N latitudes (roughly $-4500\,\text{km} \leq y \leq 4500\,\text{km}$) with a grid size of 256 points and a time step of 3 min. The climate simulations are carried for 2000 days or roughly 6 years with this perpetual summer monsoon conditions. The stochastic model is called at every time step and evolved independently over the duration of the time step using the exact algorithm of Gillespie as already mentioned. We note that this adds very little computational overhead since evolving the coarse-grained birth–death process to the next transition involves only two samples of the uniform distribution and that the effective timescales of the stochastic system are bounded from below by the transition timescales τ_{kl} in Table 4 divided by the number of lattice sites under each large-scale model gridbox, $N = n^2 = 30 \times 30$. We note that the transition times in Table 4 are inferred from large eddy simulation data representing realistic dynamics of tropical convective clouds using a rigorous Bayesian approach [9,10].

Numerical simulation results show that the stochastic monsoon circulation model has a very rich dynamics in terms of both climatology and variability [8], and which vary considerably with the choice of parameters. The model simulations exhibit some physical behavior reminiscent of the monsoon climatology [19]. We report here two cases to illustrate these results.

We consider two cases with all model parameters fixed to their standard values reported in Table 3 except for the parameter a_0 which takes the values $a_0 = 1$ and $a_0 = 3$, respectively. The parameter a_0 is an important one in the model since it parameterizes the convective response to fluctuations in the dry static buoyancy $(\theta_1 + \gamma_2\theta_2)$; increasing the magnitude of a_0 increases the effect of the dry static stability (see Table 2, closure equation for H_d), and thus reduces conditional instability [31].

In Fig. 6b, we report the root-mean-square time series of all the prognostic variables for the $a_0 = 3$ case. From this figure, we can see that the solution undergoes a transient phase of roughly 250 days (roughly three times the Newtonian damping timescale in Table 3) and then enters its statistical equilibrium and randomly oscillates around it. The oscillations have a period of roughly 25 days. This statistical equilibrium defines the new climatology for the model, which is concurrent with the imposed non uniform surface forcing.

We take the time average of this solution over the last 1000 days of the simulations and plot in Fig. 7 the climatologies associated with the two statistical steady states, corresponding to $a_0 = 1$ and $a_0 = 3$, respectively. These plots include the convective heating and cooling profiles, the three velocity component profiles, the pressure field, the potential temperature field, with the (v, w) wind vectors overlaid. Recall that the evolved baroclinic and barotropic components are the coefficients of the vertical sine and cosine expansions used in the Galerkin truncation procedure and the same basis functions are used here to reconstruct the total fields reported in Fig. 7. These pictures display many features reminiscent of the summer monsoon circulation, including a local Hadley circulation [19] with rising air in the Northern Hemisphere and sinking slightly South of the Equator consistent with the results of [2]. The rising branch coincides with the region of active deep convection marked by positive heating in the mid- and upper troposphere. The pressure field displays a region of significant pressure drop, near the surface, in the region of active convection which delimits the monsoon trough [2,19]. More importantly, the zonal wind displays an interesting twist with easterlies at the Equator, shifting to westerly South of the pressure trough and then back to easterlies. This is a signature of the reversed wind directions associated with the summer monsoon season as relayed earlier. However, there are some differences between the two runs. The main difference resides in the potential temperature profiles: While the case with $a_0 = 1$ displays warm temperature maximum in the middle of the troposphere, the case with $a_0 = 3$ has a top heavy temperature profile. Further discussion of the physical significance including the wave dynamics (deviations from this climatology) and mechanisms associated with the model parameters and

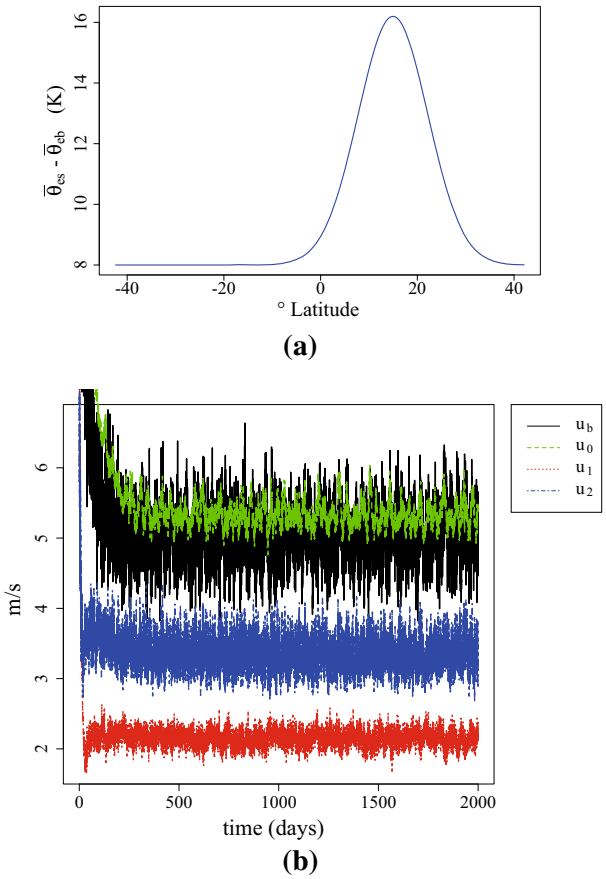

Fig. 6 **a** Imposed sea-surface temperature profile. **b** The root-mean-square time series for the zonal wind fields in the case of $a_0 = 3$

their relevance to Nature is above the scope of this paper. They will be analyzed and discussed extensively elsewhere by the authors. Nonetheless, this somehow illustrates how much complex and how much fascinating a climate model can be and exhibits some of the grand challenges faced by the climate modeling community, especially regarding the convective parameterization problem.

5 Conclusion

We presented a zonally symmetric model for the meridional circulation of the summer monsoon and the associated local Hadley circulation. The model is based on the multicloud model with a dynamically active boundary layer of Waite and Khouider [61] coupled to the stochastic convection model of Khouider et al. [27]. The dynamical core of the model is based on a systematic projection of the β-plane primitive equations of tropical dynamics onto the first three baroclinic modes of vertical structure, the vertically uniform barotropic mode and the first two baroclinic modes, in the free troposphere. The three modes are coupled with each other through advective nonlinearities and through a bulk boundary layer dynamical model that directly forces the barotropic mode through horizontal convergence. Finally, the stochastic cloud model provides the diabatic heating for the free troposphere dynamics and forces the boundary layer both dynamically and thermodynamically.

This paper discusses the design and implementation of a numerical method to solve the multimode model and its coupling to the stochastic cloud model. The coupled 4-mode model dynamical core is a nonlinear and nonconservative first-order PDE system of 13 equations, which can potentially lose hyperbolicity [57]. Inspired by previous work [28,57], we use an operator time-splitting strategy [60] where this dynamical core is divided onto three main components, a conservative system, a hyperbolic system, and a nilpotent part. The resulting initial value problem is discretized by combining, respectively, the central scheme of Nessyahu and Tadmor [50], the wave propagation method of Leveque [40], and the method of lines. Other splitting strategies

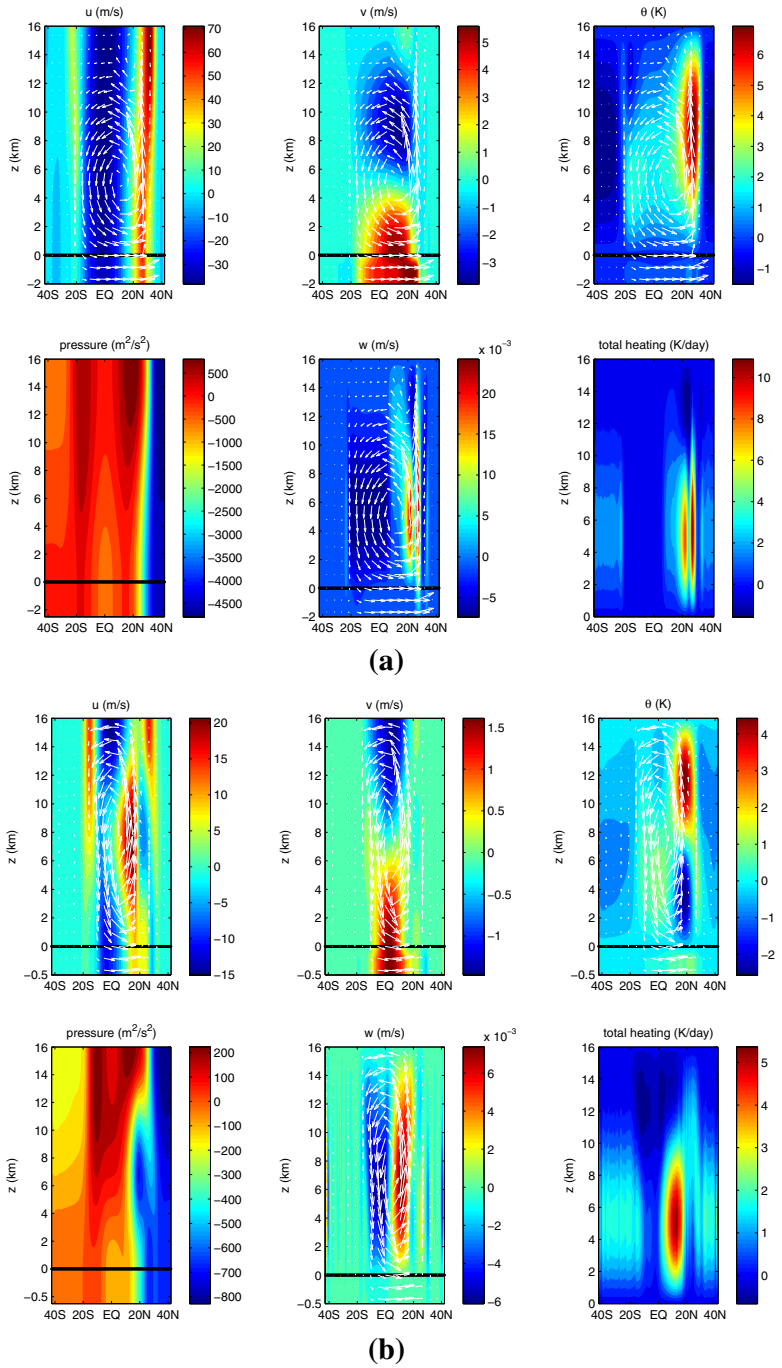

Fig. 7 Mean Hadley-monsoon circulation simulation by the coupled three vertical and ABL mode model with the stochastic convection parameterization. **a** $a_0 = 1$ and **b** $a_0 = 3$

are conceivable [7], but as demonstrated by Stechmann et al. [57], the one used here has the advantage of not blowing up even when the system is forced and driven, in phase space, toward regions of nonhyperbolicity. It is not clear whether unsplit or other splitting discretizations can pass this hard test [7].

The splitting strategy is validated using a synthetic exact solution and formal second-order convergence, under grid refinement is recovered. Finally, the dynamical core forced by the stochastic cloud model is applied to an idealized test case of monsoon conditions. The model reproduces many important features of the monsoon dynamics and the local Hadley circulation [2].

Acknowledgements The research of B.K. was partially supported by a Natural Sciences and Engineering Research Council of Canada grant and the Indian Institute for Tropical Meteorology Monsoon Mission. M.D.L.C. was partly supported through these grants as a graduate student. Computing resources are provided by WestGrid (www.westgrid.ca) and Compute Canada Calcul Canada (www.computecanada.ca).

References

1. Ajayamohan, R., Deng, Q., Khouider, B., Majda, A.J.: Role of stratiform heating on the organization of convection over the monsoon trough. Clim. Dyn. (2016). doi:10.1007/s00382-016-3033-7
2. Ajayamohan, R., Khouider, B., Majda, A.J.: Simulation of monsoon intraseasonal oscillations in a coarse-resolution aqua-planet GCM. Geophys. Res. Lett. **41**(15), 5662–5669 (2014)
3. Ajayamohan, R.S., Khouider, B., Majda, A.J.: Realistic Madden-Julian Oscillation initiation and dynamics in a general circulation model. Geophys. Res. Lett. (2013)
4. Arakawa, A.: The cumulus parameterization problem: past, present, and future. J. Clim. **17**(13), 2493–2525 (2004)
5. Batchelor, G.: An Introduction to Fluid Dynamics. Cambridge Mathematical Library, Cambridge (2000)
6. Khouider, B.: Markov-jump stochastic models for tropical convection. In: Yang, X.S. (ed.) Mathematical Modeling with Multidisciplinary Applications, pp. 471–554. Wiley, Hoboken (2013)
7. Castro-Diaz, M.J., Cheng, Y., Chernok, A., Kurganov, A.: Solving the two-mode shallow water equations using finite volume methods. Commun. Comput. Phys. **16**(5), 1323–1354 (2014)
8. De La Chevrotière, M.: Stochastic and Numerical Models for Tropical Convection and Hadley-Monsoon Dynamics. Ph.D. thesis, University of Victoria (2015)
9. De La Chevrotière, M., Khouider, B., Majda, A.J.: Calibration of the stochastic multicloud model using Bayesian inference. SIAM J. Sci. Comput. **36**(3), B538–B560 (2014)
10. De La Chevrotière, M., Khouider, B., Majda, A.J.: Stochasticity of convection in giga-les data. Clim. Dyn. **47**(5),1845–1861 (2015)
11. Deng, Q., Khouider, B., Majda, A.J.: The mjo in a coarse-resolution gcm with a stochastic multicloud parameterization. J. Atmos. Sci. **72**(1), 55–74 (2015)
12. Deng, Q., Khouider, B., Majda, A.J., Ajayamohan, R.: Effect of stratiform heating on the planetary-scale organization of tropical convection. J. Atmos. Sci. **73**(1), 371–392 (2016)
13. Dorrestijn, J., Crommelin, D.T., Siebesma, A.P., JJ, Harmen Jonker, Selten, F.: Stochastic convection parameterization with Markov chains in an intermediate-complexity GCM. J. Atmos. Sci. **73**(3), 1367–1382 (2016)
14. Drbohlav, H.K.L., Wang, B.: Mechanism of the northward-propagating intraseasonal oscillation: insights from a zonally symmetric model. J. Clim. **18**(7), 952–972 (2005)
15. Frenkel, Y., Khouider, B., Majda, A.J.: Simple multicloud models for the diurnal cycle of tropical precipitation. Part I: formulation and the case of the tropical oceans. J. Atmos. Sci. **68**(10), 2169–2190 (2011)
16. Frierson, D.M., Majda, A.J., Pauluis, O.M.: Large scale dynamics of precipitation fronts in the tropical atmosphere: a novel relaxation limit. Commun. Math. Sci. **2**(4), 591–626 (2004)
17. Gill, A.E.: Atmosphere–Ocean Dynamics. Academic Press, San Diego (1982)
18. Gillespie, D.T.: An exact method for numerically simulating the stochastic coalescence process in a cloud. J. Atmos. Sci. **32**(10), 1977–1989 (1975)
19. Goswami, B.: South Asian monsoon. In: Lau, W., Waliser, D. (eds.) Intraseasonal Variability in the Atmosphere–Ocean Climate System, pp. 21–72. Springer, Berlin (2012)
20. Goswami, B.N., Keshavamurthy, R.N., Satyan, V.: Role of barotropic, baroclinic and combined barotropic-baroclinic instability for the growth of monsoon depressions and mid-tropospheric cyclones. Proc. Ind. Acad. Sci. (Earth & Planetary Sciences) **89**, 79–97 (1980). doi:10.1007/BF02841521
21. Held, I.: The gap between simulation and understanding in climate modeling. Bull. Am. Meteorol. Soc. **86**(11) 1609–1614 (Nov. 2005)
22. Holton, J.R., Hakim, G.J.: An Introduction to Dynamic Meteorology. Academic Press, San Diego (2012)
23. Jiang, G.S., Tadmor, E.: Nonoscillatory central schemes for multidimensional hyperbolic conservation laws. SIAM J. Sci. Comput. **19**(6), 1892–1917 (1998)
24. Katsoulakis, M.A., Majda, A.J., Vlachos, D.G.: Coarse-grained stochastic processes for microscopic lattice systems. Proc. Natl. Acad. Sci. **100**(3), 782–787 (2003)
25. Khairoutdinov, M.F., Krueger, S.K., Moeng, C.H., Bogenschutz, P.A., Randall, D.A.: Large-eddy simulation of maritime deep tropical convection. J. Adv. Model. Earth Syst. **1**(4) (2009)
26. Khouider, B.: A coarse grained stochastic multi-type particle interacting model for tropical convection: nearest neighbour interactions. Commun. Math. Sci. **12**(8), 1379–1407 (2014). doi:10.4310/CMS.2014.v12.n8.a1
27. Khouider, B., Biello, J., Majda, A.J.: A stochastic multicloud model for tropical convection. Commun. Math. Sci. **8**(1), 187–216 (2010)
28. Khouider, B., Majda, A.J.: A non-oscillatory balanced scheme for an idealized tropical climate model: part I. Algortihm and validation. Theor. Comput. Fluid Dyn. **19**(5), 331–354 (2005)
29. Khouider, B., Majda, A.J.: Multicloud convective parametrizations with crude vertical structure. Theor. Comput. Fluid Dyn. **20**(5–6), 351–375 (2006)
30. Khouider, B., Majda, A.J.: A simple multicloud parameterization for convectively coupled tropical waves. Part I: linear analysis. J. Atmos. Sci. **63**(4), 1308–1323 (2006)
31. Khouider, B., Majda, A.J.: A simple multicloud parameterization for convectively coupled tropical waves. Part II: nonlinear simulations. J. Atmos. Sci. **64**(2), 381–400 (2007)
32. Khouider, B., Majda, A.J.: Multicloud models for organized tropical convection: enhanced congestus heating. J. Atmos. Sci. **65**(3), 895–914 (2008)

33. Khouider, B., Majda, A.J., Katsoulakis, M.A.: Coarse-grained stochastic models for tropical convection and climate. Proc. Natl. Acad. Sci. **100**(21), 11941–11946 (2003)
34. Khouider, B., Majda, A.J., Stechmann, S.N.: Climate science in the tropics: waves, vortices and pdes. Nonlinearity **26**(1), R1 (2013). http://stacks.iop.org/0951-7715/26/i=1/a=R1
35. Khouider, B., St-Cyr, A., Majda, A.J., Tribbia, J.: The MJO and convectively coupled waves in a coarse-resolution GCM with a simple multicloud parameterization. J. Atmos. Sci. **68**(2), 240–264 (2011)
36. Kiladis, G.N., Wheeler, M.C., Haertel, P.T., Straub, K.H., Roundy, P.E.: Convectively coupled equatorial waves. Rev. Geophys. **47**, RG2003 (2009). doi:10.1029/2008RG000,266
37. Krishnamurti, T.N., Bedi, H.S., Hardiker, V.M., Ramaswamy, L.: An Introduction to Global Spectral Modeling. Springer, Berlin (2006)
38. Lal, M., Singh, K.K., Srinivasan, G., Rathore, L.S., Naidu, D., Tripathy, C.N.: Growth and yield responses of soybean in madhyapradesh, India to climate variability and change. Agric. For. Meterol. **93**, 53 (1999)
39. Lau, W.K.M., Waliser, D.E.: Intraseasonal Variability in the Atmosphere–Ocean Climate System. Springer, Heidelberg (2005)
40. LeVeque, R.J.: Wave propagation algorithms for multidimensional hyperbolic systems. J. Comput. Phys. **131**(2), 327–353 (1997)
41. LeVeque, R.J.: Finite Volume Methods for Hyperbolic Problems, vol. 31. Cambridge University Press, Cambridge (2002)
42. LeVeque, R.J.: Finite difference methods for ordinary and partial differential equations: steady-state and time-dependent problems, vol. 98. SIAM (2007)
43. Lin, J.L., Kiladis, G.N., Mapes, B.E., Weickmann, K.M., Sperber, K.R., Lin, W., Wheeler, M.C., Schubert, S.D., Genio, A.D., Donner, L.J., Emori, S., Gueremy, J.F., Hourdin, F., Rasch, P.J., Roeckner, E., Scinocca, J.F.: Tropical intraseasonal variability in 14 IPCC AR4 climate models. Part I: convective signals. J. Clim. **19**, 2665–2690 (2006)
44. Lin, J.W.B., Neelin, J.D.: Toward stochastic deep convective parameterization in general circulation models. Geophys. Res. Lett. **30**(4), 1162 (2003)
45. Lindzen, R.S.: Dynamics in Atmospheric Physics. Cambridge University Press, Cambridge (1990). doi:10.1017/CBO9780511608285
46. Liu, P., Kajikawa, Y., Wang, B., Kitoh, A., Yasunari, T., Li, T., Annamalai, H., Fu, X., Kikuchi, K., Mizuta, R., Rajendran, K., Waliser, D.E., Kim, D.: Tropical intraseasonal variability in the MRI-20km60L AGCM. J. Clim. **22**, 2006–2022 (2009)
47. Majda, A.J.: Introduction to PDEs and Waves for the Atmosphere and Ocean, Courant Lecture Notes in Mathematics, vol. 9. American Mathematical Society, Providence (2003)
48. Moncrieff, M.W., Klinker, E.: Organized convective systems in the tropical western Pacific as a process in general circulation models: a TOGA COARE case-study. Q. J. R. Meteorol. Soc. **123**, 805–827 (1997)
49. Neelin, J.D., Zeng, N.: A quasi-equilibrium tropical circulation model-formulation. J. Atmos. Sci. **57**(11), 1741–1766 (2000)
50. Nessyahu, H., Tadmor, E.: Non-oscillatory central differencing for hyperbolic conservation laws. J. Comput. Phys. **87**(2), 408–463 (1990)
51. Organization, W.M.: Seamless Prediction of the Earth system: From Minutes to Months, vol. WMO no. 1156. World Meteorological Organization: UNESCO (2015)
52. Palmer, T.N.: A nonlinear dynamical perspective on model error: a proposal for non-local stochastic-dynamic parametrization in weather and climate prediction models. Q. J. R. Meteorol. Soc. **127**(572), 279–304 (2001)
53. Pauluis, O.: Boundary layer dynamics and cross-equatorial Hadley circulation. J. Atmos. Sci. **61**(10), 1161–1173 (2004)
54. Peters, K., Crueger, T., Jakob, C., Möbis, B.: Improved mjo-simulation in ECHAM6 by coupling a Stochastic Multicloud Model to the convection scheme. JAMES (submitted, 2016)
55. Peters, K., Jakob, C., Davies, L., Khouider, B., Majda, A.: Stochastic behaviour of tropical convection in observations and a multicloud model. J. Atmos. Sci. **70**(11), 3556–3575 (2013). doi:10.1175/JAS-D-13-031.1
56. Roache, P.J.: Quantification of uncertainty in computational fluid dynamics. Annu. Rev. Fluid Mech. **29**(1), 123–160 (1997)
57. Stechmann, S.N., Majda, A.J., Khouider, B.: Nonlinear dynamics of hydrostatic internal gravity waves. Theor. Comput. Fluid Dyn. **22**(6), 407–432 (2008)
58. Stensrud, D.J.: Parametrization Schemes: Keys to Understanding Numerical Weather Prediction Models. Cambridge University Press, Cambridge (2007)
59. Stevens, B.: Bulk boundary-layer concepts for simplified models of tropical dynamics. Theor. Comput. Fluid Dyn. **20**(5–6), 279–304 (2006)
60. Strang, G.: On the construction and comparison of difference schemes. SIAM J. Numer. Anal. **5**(3), 506–517 (1968)
61. Waite, M.L., Khouider, B.: Boundary layer dynamics in a simple model for convectively coupled gravity waves. J. Atmos. Sci. **66**(9), 2780–2795 (2009)
62. Webster, P.J.: Mechanism of monsoon low-frequency variability: surface hydrological effects. J. Atmos. Sci. **40**, 2110–2124 (1983)
63. Wheeler, M., Kiladis, G.N.: Convectively coupled equatorial waves: analysis of clouds and temperature in the wavenumber-frequency domain. J. Atmos. Sci. **56**, 374–399 (1999)
64. Yanai, M., Chen, B., Tung, W.: The Madden-Julian oscillation observed during the TOGA COARE IOP: global view. J. Atmos. Sci. **57**, 2374–2396 (2000)
65. Yoneyama, K., Zhang, C., Long, C.N.: Tracking pulses of the Madden-Julian oscillation. Bull. Am. Meteorol. Soc. (2013). doi:10.1175/BAMS-D-12-00157.1